

School of Science  
Department of Physics and Astronomy  
Master Degree in Physics

# Optoelectronic Characterization of Hybrid Organic-Inorganic Halide Perovskites for Solar Cell and X-ray Detector Applications

Supervisor:

Prof. Daniela Cavalcoli

Submitted by:

Matilde Lini

Co-supervisors:

Dr. Barbara Terheiden

Dr. Giovanni Armaroli



# Abstract

Negli ultimi 10 anni la ricerca scientifica ha volto il suo interesse verso le perovskiti alogene miste organiche-inorganiche; questo nuovo tipo di materiale si caratterizza per interessanti proprietà optoelettroniche e per la sua facilità di fabbricazione. Attualmente, trova impiego come materiale attivo in vari tipi di dispositivi, come celle solari, rivelatori di raggi X e LEDs.

Il seguente lavoro di tesi presenta la caratterizzazione di due tipi di materiali basati su perovskite. Il primo è una cella solare di metilammonio-triioduro di piombo ( $\text{MAPbI}_3$ ) in forma di film sottile. Questo dispositivo è stato fabbricato e caratterizzato presso l'Università di Costanza (Germania), con l'obiettivo di migliorarne la procedura di deposizione. Il secondo materiale studiato è un cristallo singolo di metilammonio-tribromuro di piombo ( $\text{MAPbBr}_3$ ); lo si è caratterizzato presso l'Università di Bologna tramite spettroscopia di fotovoltaggio superficiale e spettroscopia di fotocorrente, in funzione della dose di fotoni X depositati, in modo da verificarne gli effetti indotti.

In seguito all'esposizione di raggi X, l'energia di legame degli eccitoni, così come risulta dagli spettri di fotovoltaggio superficiale, subisce un incremento pari a 20 meV rispetto al campione non irraggiato. L'osservazione degli spettri di fotocorrente ha portato alla medesima conclusione. Le motivazioni dell'osservato incremento di energia sono state discusse e attribuite ad un cambiamento di polarizzabilità del cristallo singolo. La successiva caratterizzazione dopo diverse ore dall'ultimo irraggiamento dimostra che il materiale recupera le sue condizioni iniziali.



# Abstract

In the last 10 years, the research interest has been drawn towards the hybrid organic-inorganic halide perovskites, an innovative material characterized by remarkable optoelectronic properties and by its simplicity of fabrication; hybrid halide perovskites are currently being employed as active material in solar cells, X-ray photodetectors and light emitting devices.

The following thesis presents the characterization of two perovskite-based materials. The first is a methylammonium lead iodide ( $\text{MAPbI}_3$ ) thin film solar cell, which has been fabricated and characterized at the University of Konstanz (Germany), with the aim to optimize the deposition procedure. The second material is a methylammonium lead bromide ( $\text{MAPbBr}_3$ ) single crystal that have been characterized at the University of Bologna with surface photovoltage and photocurrent spectroscopies, as a function of the deposited dose of X-rays in order to monitor the induced effects of radiation.

After the exposure to X-rays, the exciton binding energy, calculated from the surface photovoltage spectra, has been found to increase by 20 meV with respect to the not irradiated sample. A similar result has been found with the photocurrent spectroscopy. The reasons for the increase in binding energy is discussed and attributed to a change in polarizability of the single crystal. The recovery of the crystals has been registered as well and has shown that the material is able to return to the initial condition after just few hours from the last X-ray's deposition.



# Contents

<b>Introduction</b>	<b>1</b>
<b>1 Hybrid Organic-Inorganic Halide Perovskites</b>	<b>3</b>
1.1 Hystory and first optoelectronic applications . . . . .	3
1.2 Atomic structure and phases . . . . .	4
1.3 Optoelectronic properties . . . . .	8
1.3.1 Band structure . . . . .	8
1.3.2 Mobility and charge transport properties . . . . .	9
1.3.3 Light absorption . . . . .	10
1.4 Applications . . . . .	15
1.4.1 Perovskite solar cells . . . . .	15
1.4.2 X-ray radiation photodetectors . . . . .	19
1.5 Defects, stability and health issues . . . . .	22
1.5.1 Defects . . . . .	22
1.5.2 Stability . . . . .	24
1.5.3 Health issues . . . . .	26
<b>2 Experimental methods</b>	<b>27</b>
2.1 Sample growth . . . . .	27
2.1.1 MAPbI <sub>3</sub> solar cells . . . . .	28
2.1.2 MAPbBr <sub>3</sub> single crystals . . . . .	29
2.2 Characterization techniques . . . . .	32
2.2.1 Photovoltaic characterization . . . . .	32
2.2.2 Surface photovoltage spectroscopy . . . . .	33
2.2.3 Photocurrent spectroscopy . . . . .	37
2.2.4 X-ray irradiation setup . . . . .	38

---

<b>3</b>	<b>Optoelectronic characterization results</b>	<b>41</b>
3.1	MAPbI <sub>3</sub> photovoltaic characterization . . . . .	41
3.2	MAPbBr <sub>3</sub> optoelectronic characterization . . . . .	43
3.2.1	Surface photovoltage spectroscopy . . . . .	43
3.2.2	Current - voltage characterization . . . . .	51
3.2.3	Photocurrent spectroscopy . . . . .	52
3.2.4	Comparison between Surface photovoltage and Photocurrent measurements . . . . .	53
3.3	MAPbBr <sub>3</sub> X-ray hardness characterization . . . . .	56
3.3.1	Surface photovoltage spectroscopy . . . . .	57
3.3.2	Photocurrent spectroscopy . . . . .	64
3.3.3	Comparison between Surface photovoltage and Photocurrent measurements . . . . .	65
3.3.4	Discussion on the increase of exciton binding energy . . . . .	68
	<b>Conclusions</b>	<b>71</b>
	<b>Bibliography</b>	<b>75</b>

# Introduction

The hybrid organic-inorganic halide perovskites are an innovative type of material with general composition  $ABX_3$ , where A is an organic cation, usually methylammonium or formamidinium, B is an inorganic cation, usually lead or tin, and X is a halogen anion, iodine, bromine or chlorine.

The material is marked by excellent transport properties; moreover, the substitution of the halide component allows to tune the magnitude of the band gap. Thanks also to the simplicity and affordability of fabrication, hybrid halide perovskites are widely applied as active materials in solar cells, whose efficiency has reached up to 25% [1]. Hybrid perovskites are also employed as detectors for X-ray radiation, on account of the high stopping power of heavier elements such as lead [2, 3].

The study on the nature and on the behaviour of the photogenerated species in halide perovskites is fundamental. It is known that the photoexcitation in halide perovskites gives rise, quite immediately, to free charge carriers at room temperature [4]; the immediate generation of free charges is attributed to the low binding energy of excitons, which are neutral quasi-particles formed by the electrostatic interaction between an electron and a hole. This is one of the reasons why the optoelectronic performance of halide perovskites is comparable to the one of conventional inorganic semiconductors such as silicon. Nonetheless, depending both on the experimental method and on the material's form, whether polycrystalline or single crystal, the value for the exciton binding energy reported in literature ranges widely from tens to hundreds of meV [5]. Moreover, excitons are responsible for the large absorption coefficient close to the band gap, and the exciton's recombination, rather than free charges recombination, is considered to be the main source of photoemission in perovskites [6]. This suggests that excitons and free carriers can coexist and that excitons should not be neglected in regards of the optoelectronic properties of the material.

With respect to their application as X-ray detectors, it is crucial to perform radiation hardness tests, by irradiating the material with ionizing photons and monitoring the effects as a function of the deposited dose and the subsequent recovery with time; in

fact, a fundamental requirement for ionizing radiation detectors is whether high doses are tolerated and, if there are relevant effects induced by the radiation, whether the material recovers fastly its initial condition.

In this regard, this work presents the characterization of a MAPbI<sub>3</sub> thin film solar cell with the aim of optimizing the photovoltaic parameters and successively test its radiation hardness with X-rays. However, because of the Covid-19 emergency and the subsequent closure of the university, it was not possible to deepen the research and to test the solar cells under X-rays. The radiation hardness measurements has been instead performed on MAPbBr<sub>3</sub> single crystals, which recently have shown interesting applications as X-ray detectors [2].

This thesis is structured in three chapters:

**Chapter one** is focused on the material and its optoelectronic properties, with particular stress on the role of excitons; a description of the two cited applications, solar cell and X-ray photodetector is also given. The chapter concludes the discussion with some examples of issues related to halide perovskites, such as defects, stability and health related risks.

**Chapter two** is dedicated to the experimental methods that have been employed to fabricate the thin film MAPbI<sub>3</sub> solar cells and the single crystals MAPbBr<sub>3</sub>; the experimental setup for the solar cell's characterization and the techniques of the surface photovoltage and photocurrent spectroscopies are also presented, along with the X-ray tube that has been used.

**Chapter three** presents an example of photovoltaic characterization of the MAPbI<sub>3</sub> solar cells, with the related photovoltaic parameters; the results of the surface photovoltage and photocurrent spectroscopies on the MAPbBr<sub>3</sub> single crystals have been analysed before and after X-ray exposure. The final part of the chapter contains the analysis and the discussion on the possible interpretations of the results.

# Chapter 1

## Hybrid Organic-Inorganic Halide Perovskites

The name *perovskite* identifies a group of compounds with the same structure as the mineral  $\text{CaTiO}_3$ . The general stoichiometry formula for those materials is  $\text{ABX}_3$ , where A and B are two cations with generally different dimensions and X is the anion.

The perovskite crystal structure can be found in many materials, both natural and synthetic. The most historically studied were the oxide perovskites.

Nowadays, the most used perovskites for device applications are hybrid organic-inorganic halide perovskites, composed by a monovalent cation that can be organic (usually methylammonium or formamidinium) or inorganic (usually alkali metals like cesium), by a smaller divalent cation (usually lead or tin) and by a halogen anion (iodine, bromine or chlorine).

### 1.1 History and first optoelectronic applications

The mineral calcium titanate  $\text{CaTiO}_3$  was discovered by the german scientist Gustav Rose in 1839 during a trip to Russia in Urali mountains and named “perovskite” in honour of Count Lev A. von Perovski, a mineralogist who served as the Minister of Internal Affairs under Nicholas I of Russia.

The interest in perovskite research came in 1920s, when the norwegian scientist Victor Goldschmidt issued a detailed study on the structure of  $\text{CaTiO}_3$ , with the development of the so called *tolerance factor*, a parameter that determines whether a crystal presents in a perovskite structure or not [7].

Oxide perovskites, like calcium and barium titanate, were employed in a variety of products like condensers, transducers and other devices since they showed superior ferroelec-

tric, magnetic and superconductive properties [8].

The development of the first lead halide perovskite in aqueous solution was made by H. L. Wells in 1892, with cesium as the A cation [9]. But only in 1958 Møller determined its crystallographic structure and also observed the material's conductivity [10]. The first hybrid organic-inorganic perovskite was made in 1978 by D. Weber who replaced cesium with the organic cation methylammonium [11].

D.B. Mitzi in the 1990s reported the first use of organic-inorganic halide perovskites in LEDs and thin film transistors [12].

The use of lead halide perovskites in photovoltaics became possible thanks to the pioneering work of M. Grätzel, the inventor of electrolyte-based dye-sensitized solar cells (DSSC); in 2009, the group of Miyasaka used methylammonium lead halide as a sensitizer in DSSC, reaching 3.8% of efficiency [13]. In the same year, Park and co-workers were able to obtain higher efficiency by changing the electrolyte formulation of the DSSC and the deposition of perovskite sensitizer in the form of nanoparticles, however the device suffered by poor stability [14].

Few years later, in 2012, Grätzel and Park together published a paper where the liquid electrolyte was replaced with a solid state hole conductor and perovskite as the sensitizer. The use of a solid hole conductor material solved the stability problems of liquid sensitized cells and allowed them to reach 9.7% of efficiency [15].

In the same year, the group of Miyasaka and Snaith realized the first full-solid state device by depositing a thin layer of perovskite. This work revealed that perovskite could not be just used as a sensitizer, and that it was able to transport both electrons and holes [16].

Nowadays, perovskite solar cells have reached up to 25% of efficiency, being the most rapid growing solar cell technology in the last 10 years [1].

## 1.2 Atomic structure and phases

The ideal crystal structure for hybrid organic-inorganic halide perovskite  $ABX_3$  is cubic [11], where  $BX_6$  forms an octahedron with B located at the center, while the A cation occupies the cuboctahedral voids as shown in figure 1.1. The stability of the crystal structure is described by the Goldschmidt's *tolerance factor* [7]:

$$t = \frac{R_A + R_X}{\sqrt{2}(R_B + R_X)} \quad (1.1)$$

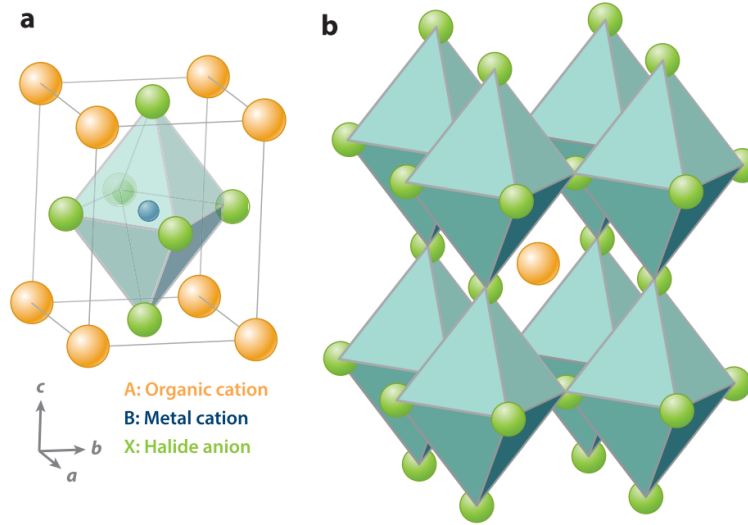


Figure 1.1: (a): Unit cell of a cubic perovskite. The organic cations (orange) occupy the lattice corners, the inorganic cations (blue) occupy the center, the anions (green) occupy the lattice faces. (b): Alternative view of the perovskite structure where  $BX_6$  form the octahedra while the organic cations occupy the voids. From [17].

where  $R_A$ ,  $R_B$  and  $R_X$  are the radii of A, B and X respectively. For halide perovskite ( $X=Cl, Br, I$ ), the tolerance factor spans from 0.81 to 1.11 [19]. When  $t$  lies between 0.89 and 1.0, the perovskite is in cubic structure. The cubic symmetry is the ideal case for perovskites since it presents higher electronic properties. When  $t$  is in the lower range, the structure is less symmetric due to a compression of the B-X bonds; in this case each octahedron tilts and the structure goes from cubic to tetragonal and to orthorhombic. On the other hand, when  $t \gg 1$ , the A cation is too large to allow the 3D structure to be stable and the perovskite presents itself in layered 2D structures or 1D chains. In addition to the tolerance factor, Li et al.[18] developed the *octahedral factor* to dictate the stability of the  $BX_6$  octahedron. The octahedral factor is given by the ratio between the ionic radius of B and X:

$$\mu = R_B/R_X \quad (1.2)$$

The halide perovskite structure occurs for  $\mu > 0.442$ . Below this value the octahedron becomes unstable and the perovskite structure will not form. Both tolerance and octahedral factors are not sufficient to predict the formation of all perovskite structures, however they provide a general criteria to determine the crystalline symmetry. Tolerance and octahedral factor for 12 different perovskites are reported in figure 1.2 [19].

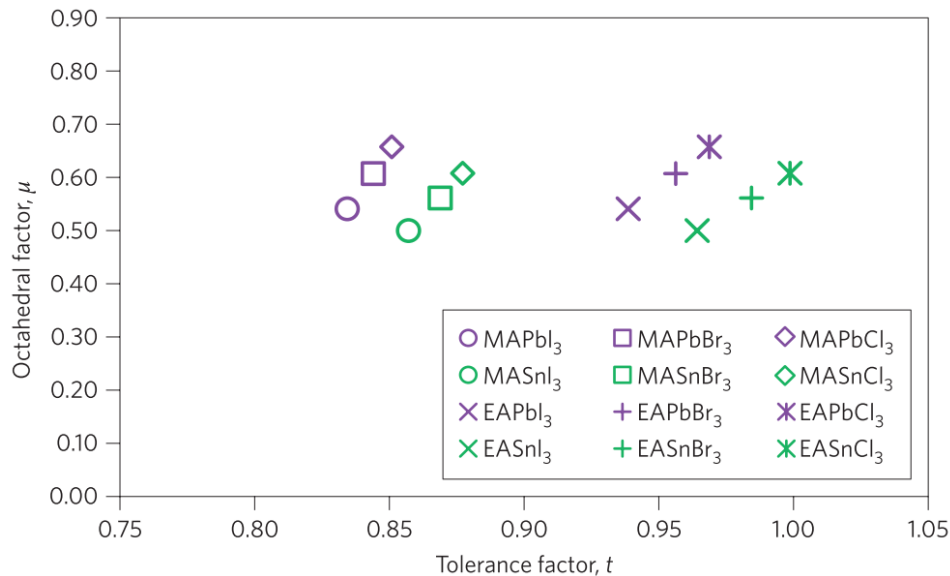


Figure 1.2: Calculated  $t$  and  $\mu$  for 12 halide perovskites (MA: methylammonium, EA: ethylammonium), from [19].

### Organic-inorganic halide perovskites

In hybrid organic-inorganic halide perovskite, the A monovalent cation is an organic composite like the methylammonium ion  $\text{CH}_3\text{NH}_3^+$  (commonly called MA) or formamidinium ( $\text{HC}(\text{NH}_2)_2^+$ , FA), which is slightly larger. Also inorganic cations like the smaller  $\text{Cs}^+$  with respect to MA or FA is often used. The A cation generally does not affect the atomic structure and therefore does not directly contribute to the electronic properties at the band edge. However, when increasing its size, the bond between the B cation and X anion can stretch, leading to a tilt in the  $\text{BX}_6$  octahedra which ultimately acts on the band structure and on the band gap.

The smaller divalent cation, B, is usually lead, which allows to reach higher performance and stability. Tin is also used as a non-toxic replacement. Tin makes the band gap smaller, however tin based perovskite are not so stable [20]. Replacing lead would also be favourable from a commercialization perspective since many countries have banned its use.

The X halogen anion can be iodide, bromide or chloride. From I to Cl the size decreases so the band gap increases. The ability to tune the band gap by anion substitution is considered one of the biggest advantages of halide perovskites. Moreover, the electronegativity will increase so that the bond between the B and X will increase the ionic and decrease the covalent character.

Mixed compositions are also possible. Mixing cations and halides stabilize the perovskite

lattice, by increasing the formation energy of defects and thus increasing the device performances. The triple-cation Cs/MA/FA perovskite for solar cells application is one the most stable compositions [21].

### Phase transitions

The three-dimensional lead halide perovskites has several phases. The  $\text{MAPbI}_3$  has four solid phases: cubic, tetragonal, orthorhombic and a non-perovskite phase. At high temperature ( $T > 327$  K),  $\text{MAPbI}_3$  is found in the cubic phase. Below 327 K, it undergoes a phase transition to the tetragonal phase. In the cubic and the tetragonal phase the MA cations are disordered and upon application of an electric field, they can reorient, giving a high ferroelectric response. When going from cubic to tetragonal, the octahedral tilt and the unit cell doubles its length. Below 162K, the  $\text{MAPbI}_3$  goes into the orthorhombic phase, where the MA cations are ordered. The transition to the non-perovskite phase occurs only in presence of solvents [22].

Due to the smaller radius of bromide with respect to iodide, the bromide perovskite,  $\text{MAPbBr}_3$ , has a cubic structure at room temperature. In this case, the MA cation rotates in high temperature phases while lowering the temperature and going from cubic to tetragonal (below 230 K) to orthorhombic phases (below 150 K), the rotation decreases [23]. The chloride perovskite is also found in a cubic structure at room temperature, with a transition to the tetragonal phase at lower temperature.

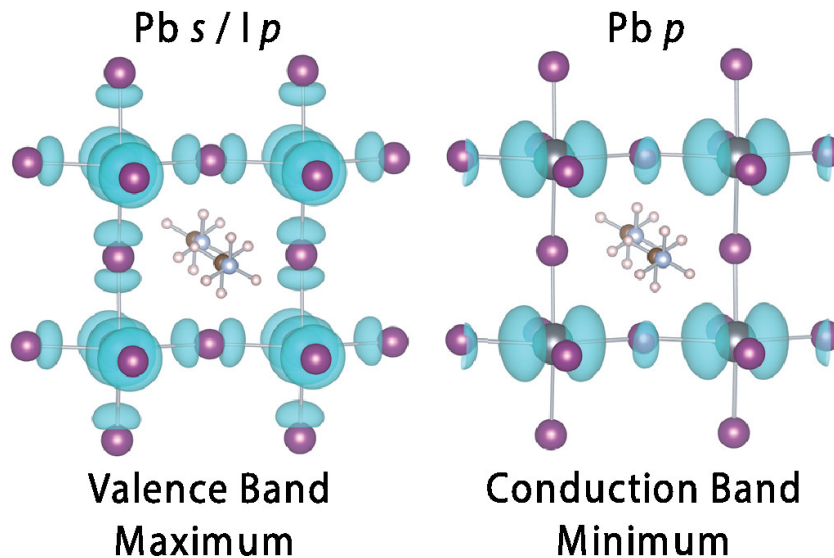


Figure 1.3: Isosurface plot of the electron density associated to the wavefunctions of the upper valence and lower conduction bands of MAPbI<sub>3</sub>. From [25].

## 1.3 Optoelectronic properties

The optoelectronic properties of lead halide perovskites include the band-gap tunability upon substitution of the halogen atom, high absorption coefficient, high charge carriers mobility and long diffusion lengths.

### 1.3.1 Band structure

In hybrid lead halide perovskites, the maximum of the valence band is formed by the antibonding states derived from hybridization of the atomic halide p-orbitals with the lead 6s-orbitals. Whereas the conduction band minimum is formed of empty 6p orbitals of lead [24]. The electron density of the wavefunctions of MAPbI<sub>3</sub> is presented in figure 1.3.

Band states are deeply affected by the substitution of the halide component: the valence band comes from the hybridization of the 6s orbital of the lead with the 5p or 4p or 3p when substituting iodide with bromide or with chloride respectively; from substitution of a smaller halogen, the lattice parameter reduces and, as a consequence, the overlap between the wavefunctions increases thus increasing the orbital coupling and the band gap [26].

As already mentioned, the organic cation does not contribute significantly to the energy band structure. In fact, the MA electronic levels lie deep within the valence and conduction band. However, the dimension of the organic cation can change the band structure

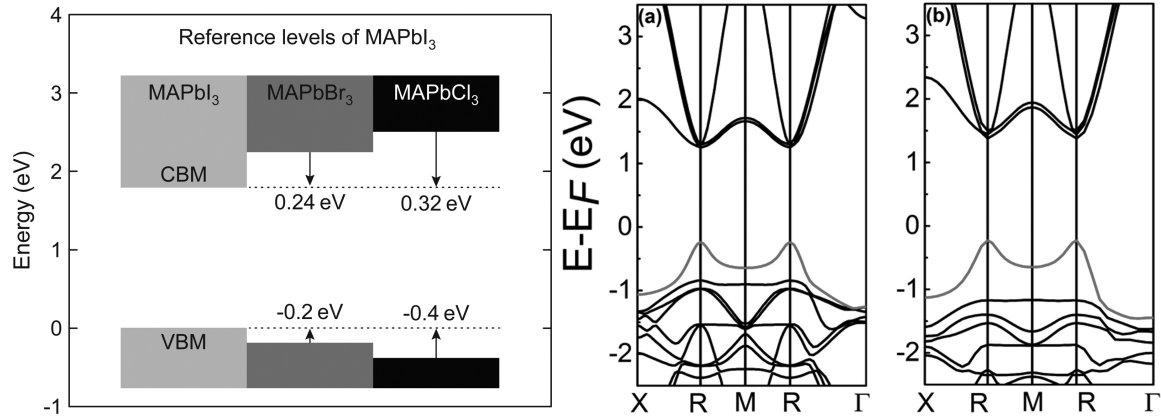


Figure 1.4: Left: Band-gap increasing upon substitution of iodine with bromine and chlorine, from [26]. Right: Calculated band structure for  $\text{MAPbI}_3$  (a) and  $\text{MAPbBr}_3$  (b), from [27]. The difference in the valence band is due to a stronger s-p bonding in the bromide perovskite, caused by a shorter Pb-Br bond length.

indirectly: slightly larger A cations can distort the B-X bond. Also the orientation of the organic cation from  $\langle 100 \rangle$  to  $\langle 111 \rangle$  can affect as well the octahedral cage, leading to a shift from direct to indirect band gap [28].

Due to the heavy nature of lead ions, the spin-orbit coupling should be considered in calculation of the band gap. The inclusion of such interaction give rise to the Rashba effect, which consists in a splitting of the conduction band and a consequent indirect nature of the band gap. This can be relevant for bromide, but insignificant for chloride perovskite [29].

### 1.3.2 Mobility and charge transport properties

#### Effective mass

The effective mass of holes and electrons can be assessed from first-principle calculations of the band curvature or experimentally, for example from magneto-absorption measurements. The effective masses for holes and electrons in  $\text{MAPbBr}_3$  were first calculated by Park and Chang to be  $m_e^* = 0.25m_0$  for electrons and  $m_h^* = 0.12m_0$  for holes [30]. The value of the effective mass changes lightly depending on how the band structure is calculated or on the particular composition of the perovskite, which give rise to different curvature. These effective masses are remarkably comparable with those of inorganic semiconductors like GaAs which has  $m_e^* = 0.066m_0$  for electrons,  $m_{hh}^* = 0.5m_0$  for heavy holes and  $m_{lh}^* = 0.08m_0$  for light holes.

## Charge-carrier mobility

Despite the similar effective masses, the charge carrier mobility is lower with respect to that of inorganic semiconductors. In the semiclassical transport model, the mobility is defined by  $\mu = \frac{e\tau}{m^*}$ , being  $m^*$  the effective mass of electrons or holes and  $\tau$  the momentum relaxation time.  $\tau$  is the average time interval between two scattering events that lead to a randomization of the charge carrier velocity with respect to the ohmic conduction.

The relaxation time constant is determined by scattering mechanisms, both intrinsic and extrinsic, occurring in the material.

The intrinsic scattering mechanisms involve the interaction between the charge and the lattice. In polar semiconductors, like hybrid halide perovskites, the charges and the polarized medium are coupled to form a quasi-particle called polarons. Carriers "dressed" by the local lattice polarization drag the field through the crystal thus being slowed and exhibiting a lower mobility [17].

The interaction with longitudinal optical phonons is characterized by the Fröhlich coupling constant. Fröhlich interactions are found to be enhanced in Br perovskite with respect to I perovskites, due to a higher ionicity of the Pb-Br bond with respect to the Pb-I bond.

The intrinsic electron-phonon coupling sets a limit to the maximum attainable charge carrier mobilities, however, also extrinsic factors contribute in lowering the charge carrier mobilities. Those extrinsic effects include scattering by grain boundaries, dopants, disordered energy landscape.

The grain size is one of the most relevant factors: the charge carrier mobility is increased from a poly-crystalline thin film to a single crystal.

### 1.3.3 Light absorption

The absorption coefficient describes how light is absorbed in the material as a function of the photon energy. The absorption of hybrid halide perovskites is characterized by a sharp onset, comparable with that of inorganic semiconductors, as shown in figure 1.5.

#### Light absorption in presence of excitons

Excitons are believed to be responsible for the large absorption coefficient close to the band gap. Excitons are neutral quasi-particle formed by an electron and a hole electrostatically bounded. The value of the exciton binding energy is particularly relevant for both radiation detectors and solar cells where excitons must be efficiently dissociated

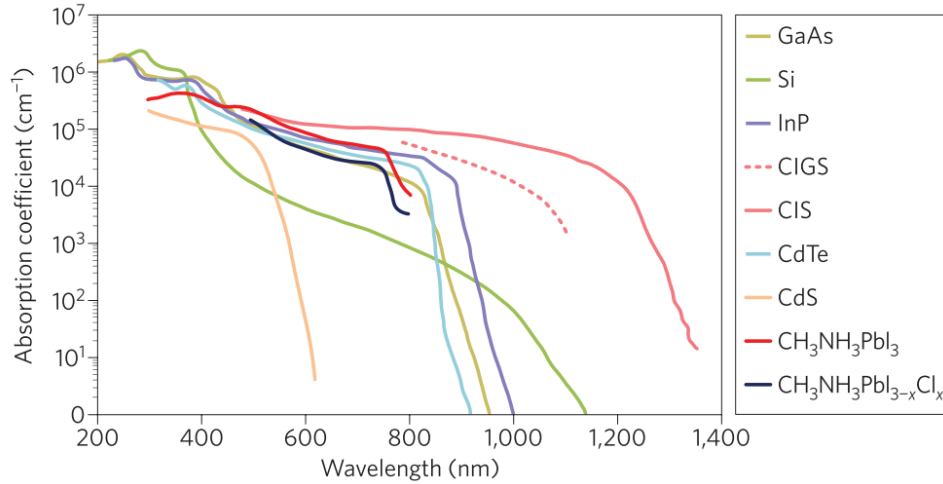


Figure 1.5: Comparison of the absorption coefficient between inorganic semiconductors commonly used in solar cells and lead halide perovskites. From [19].

in free charge carriers to be collected at the electrodes.

In inorganic semiconductors, the exciton binding energy is low enough to allow the separation of the pair quite immediately with the absorption of light, thus creating free charge carriers at room temperature. Those kind of particles are called “Wannier” excitons, characterized by a low binding energy and radius exceeding several lattice constants; for these reasons are also called free excitons.

On the other hand, in organic semiconductors, light does not create immediately free charges, as excitons can have binding energy much larger than the thermal energy. Those excitons are called “Frenkel” excitons, characterized by a large binding energy and a small radius; they are also called bound excitons since are strongly localized.

It is believed that excitons in halide perovskites have sufficiently low energy to be described within the Wannier-Mott model. The electron-hole couple is assimilated to an hydrogen atom with reduced mass  $\mu$  moving in a polarizable medium with dielectric function  $\epsilon_r$  leading to bound energy states:

$$E_n = E_g - \frac{E_b}{n^2} \quad (1.3)$$

$$E_b = \frac{R_0 \mu}{m_0 \epsilon_r^2} \quad (1.4)$$

where  $R_0 = 13.6eV$  is the Rydberg constant,  $\mu^{-1} = m_e^{*-1} + m_h^{*-1}$  is the reduced exciton mass, expressed in unit of the electron mass  $m_0$  and  $n$  is the principal quantum number of the exciton state.

Within the Wannier model, the behaviour of the absorption coefficient in presence of

excitons is described by the Elliott formula [32, 33]:

$$\alpha(\hbar\omega) \propto \frac{\mu_{cv}^2}{\hbar\omega} \left[ \sum_n \frac{4\pi\sqrt{E_b^3}}{n^3} \delta(\hbar\omega - E_g + E_b/n^2) + \frac{2\pi\sqrt{E_b}\Theta(\hbar\omega - E_g)}{1 - e^{-2\pi\sqrt{\frac{E_b}{\hbar\omega - E_g}}}} \right] \quad (1.5)$$

where  $\mu_{cv}$  is a constant related to the transition dipole moment,  $\hbar\omega$  is the photon energy.  $\delta$  and  $\Theta$  are the Dirac-delta and Heaviside step functions.

The absorption is composed by two terms:

- The exciton absorption, characterized by delta-peaks centered at the exciton energy. The absorption intensity of each n-th level is reduced by  $1/n^3$ .
- The continuum absorption, which does not simply follow the square dependence on the density of states with energy but is enhanced by the Coulomb interaction.

Temperature and disorder effects broaden the discrete energy levels; to account for such effects, both excitonic and continuum absorption are convoluted with a bell-shaped function:

$$\alpha(\hbar\omega) \propto \frac{\mu_{cv}^2}{\hbar\omega} \left[ \sum_n \frac{2E_b}{n^3} g\left(\frac{\hbar\omega - E_g + E_b/n}{\Gamma}\right) + \int_{E_g}^{\infty} g\left(\frac{\hbar\omega - E}{\Gamma}\right) \frac{1}{1 - e^{-2\pi\sqrt{\frac{E_b}{E - E_g}}}} \frac{1}{1 - \frac{8\mu b}{\hbar^3}(E - E_g)} dE \right] \quad (1.6)$$

$\Gamma$  is the linewidth and the term  $8\mu b/\hbar^3$  is a small correction to account for the non-parabolicity of the bands. The behaviour of equation 1.6 is reported in figure 1.6.

It is experimentally evident that upon substitution of I with Br, not only the energy gap, but also the binding energy of the exciton increases as reported in figure 1.7. The reason for the increase of the exciton binding energy as the band gap increases can be found in a decrease of the dielectric function. Glaser et al. [34] evaluated the optical dielectric function of  $\text{MAPbX}_3$  and found a decrease in polarizability in the series I-Br-Cl ( $\epsilon_r(I) = 5.0$ ,  $\epsilon_r(Br) = 4.7$ ,  $\epsilon_r(Cl) = 4.0$ ). The polarization is responsible for the screening of the Coulombic interaction between electrons and holes by means of the dielectric function which describes the response of a material to an external electric field. The real part of a typical dielectric function of  $\text{MAPbI}_3$  is reported in figure 1.8. The dielectric function is governed by four main contributions:

- On the high frequency part, the electronic interband transitions is responsible for the sharp onset followed by the quasi-static response  $\epsilon_s^{optical}$ .

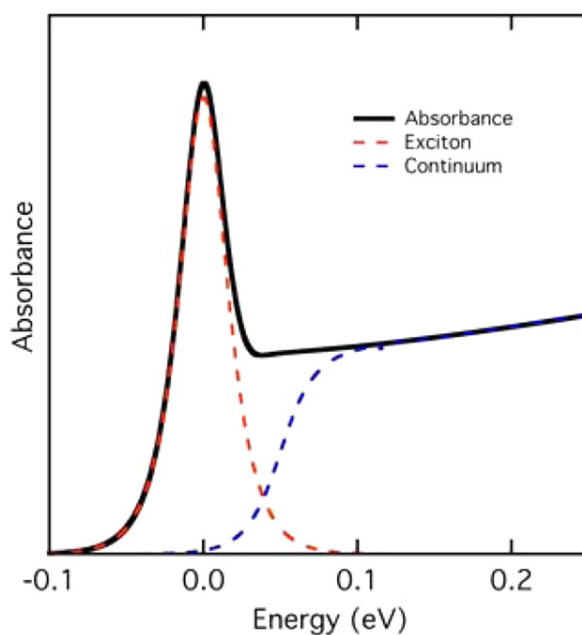


Figure 1.6: Absorption spectrum computed according to the formula 1.6. The black line is the absorption spectrum computed according to Elliott formula based on parameters typical of MAPbBr<sub>3</sub> ( $E_b = 50$  meV,  $\Gamma = 14$  meV,  $E_g = 2.3$  eV,  $8\mu b/\hbar^3 = 0.091\text{eV}^{-1}$ ), with the two contributions from exciton and continuum states, respectively, represented by the red and blue dashed lines. From [33].

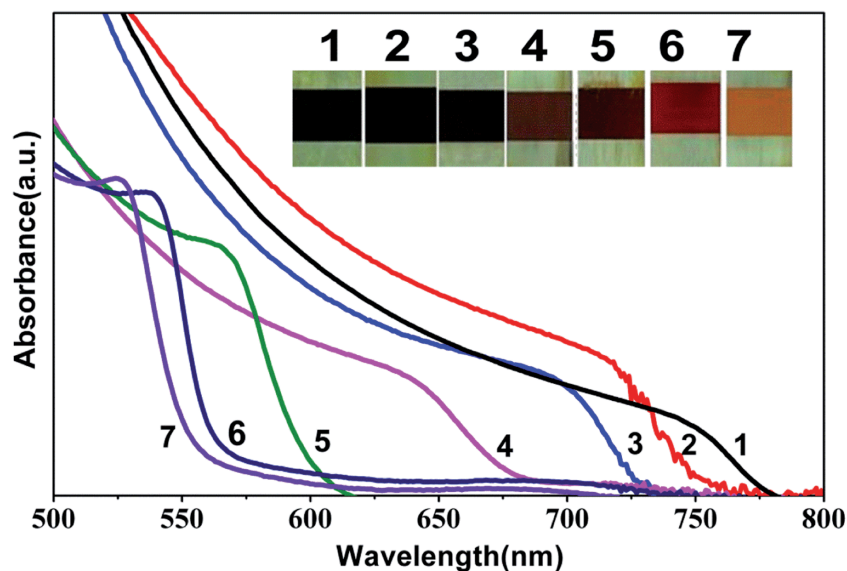


Figure 1.7: Absorption spectra for lead halide perovskite with varying I to Br ratio (MAPb(I<sub>1-x</sub>Br<sub>x</sub>)<sub>3</sub>). Sample and spectrum number 1 refers to all iodide, while the number 7 refers to all bromide content. From [31].

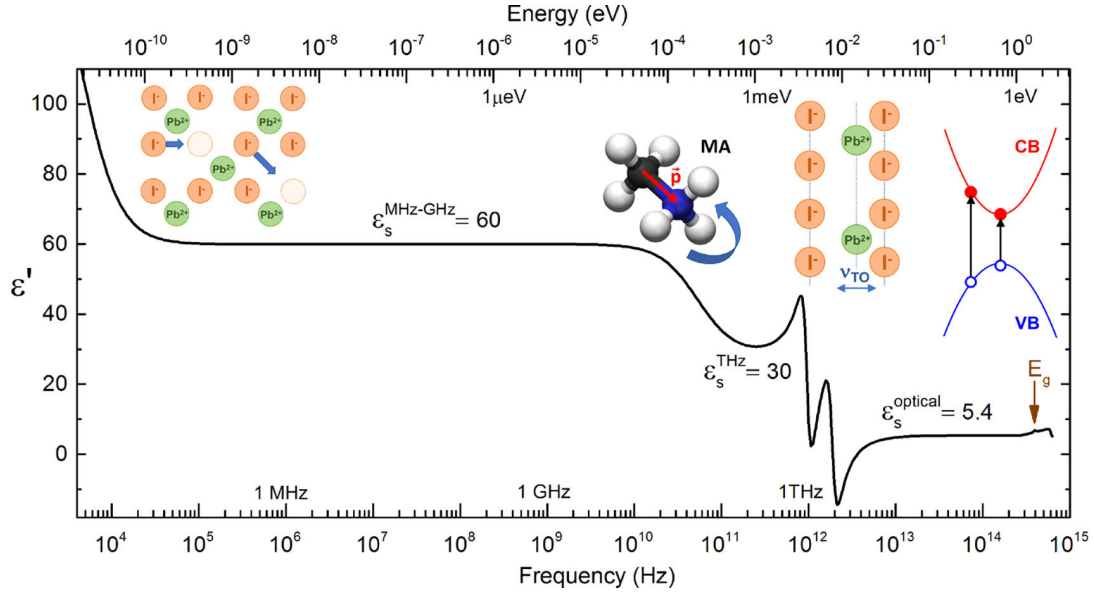


Figure 1.8: Behaviour of the real part of the dielectric function with frequency of the applied electric field. From [17].

- Toward lower frequencies, polar vibrations of optical phonons of the lead-halide cage determine the resonances around 1-2 THz ending up in a quasi-static dielectric function  $\epsilon_s^{THz}$ .
- Below 100 GHz, there is the contribution of the rotational motion of the organic cation MA, leading to a dielectric function  $\epsilon_s^{MHz-GHz}$ .
- In the low-frequency edge the dielectric function increases because of the migration of slow ions.

It is evident from figure 1.8 that the value of the exciton binding energy depends on what dielectric function is used to calculate 1.4.

A polarization response whose energy falls below  $E_b$  do not contribute to the screening since it can not follow the motion of the electron-hole pair. As suggested in [17], one can evaluate the exciton binding energy from direct measurements like magneto-absorption technique or analysis of the shape of the optical absorption and take as  $\epsilon_r$  an effective value  $\epsilon_{eff} = \epsilon_r(E_b)$ . For exciton binding energies like the one of figure 1.6, one should consider the dielectric function evaluated at around 50 meV, which in this case falls in the range of the ionic and band-to-band contributions.

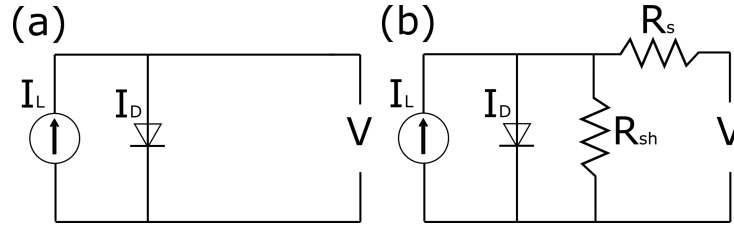


Figure 1.9: Equivalent circuit for an ideal solar cell (a), and for a real solar cell (b).

## 1.4 Applications

Lead halide perovskites are mostly employed as active layer in solar cells, but also in light emitting devices such as LEDs, lasers and photodetectors.

In the following sections, the solar cell and photodetector structures will be described.

### 1.4.1 Perovskite solar cells

#### Solar cell working principle

Solar cells are electrical devices able to convert sunlight into electricity, exploiting the photovoltaic effect in which an impinging photon, with energy at least equal to the material's energy gap, creates an electron-hole pair. The pair is successively separated by an internal field and collected.

A solar cell is basically a p-n junction and an efficient solar cell shows a good diode behaviour in dark condition, represented by the blue curve in figure 1.10. When the junction is illuminated, the solar cell can be represented by an equivalent circuit, reported in figure 1.9 (a), made of a current generator, which provides the photogenerated current  $I_L$  and of a diode, which provides the current  $I_D$ .

The total current going through the circuit is given by the sum of the diode current and the current of the generator, expressed by:

$$I = I_0(e^{qV/nk_bT} - 1) - I_L \quad (1.7)$$

where  $I_0$  is the reverse diode current,  $q$  is the electronic charge,  $n$  is the ideality factor of the diode,  $k_b$  is the Boltzmann constant and  $T$  is the temperature. The I-V characteristic under illumination shifts down with respect to the dark behaviour, as depicted by the red curve in figure 1.10. The maximum power generated by a solar cell,  $P_{max}$ , is negative, meaning that the device correctly provides power instead of requiring it.

The short-circuit current,  $I_{sc}$ , is defined as the current when the voltage across the solar

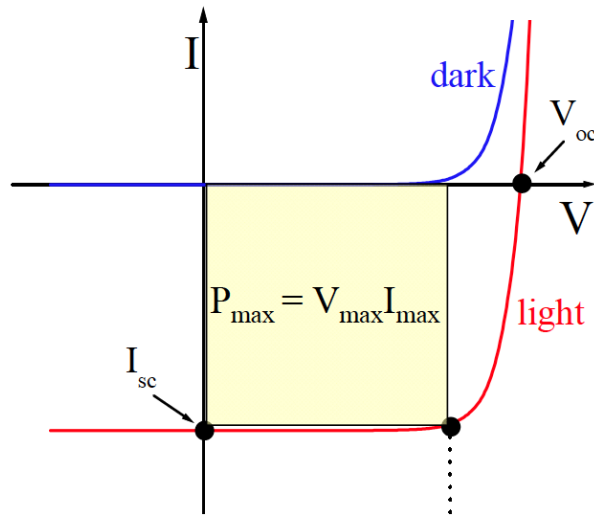


Figure 1.10: I-V curve of a solar cell in dark (blue curve) and in light condition (red curve).  $V_{oc}$  and  $I_{sc}$  are respectively the open circuit voltage and the short circuit current.  $P_{max}$  is the maximum power photogenerated. With respect to the dark, the characteristic of the solar cell under illumination shifts to the IV quadrant.

cell is zero.  $I_{sc}$  is due to the generation and collection of electron-hole pairs and it is the maximum current available for a solar cell.

The open-circuit voltage,  $V_{oc}$ , is defined as the voltage when the current across the solar cell is zero. It is the maximum voltage available for a solar cell.

Several factors contribute to deteriorate the performance of a solar cell. Non-ideality mechanisms are described introducing two resistivities: the series ( $R_s$ ) and the shunt ( $R_{sh}$ ) resistances; both modifies the equivalent circuit as shown in figure 1.9 (b). In this case, the total current flowing through the circuit as a function of the voltage can be written as:

$$I = I_0(e^{qV - qIR_s/nk_bT} - 1) - I_L + \frac{V - IR_s}{R_{sh}} \quad (1.8)$$

The shunt resistance and the series resistance modify the I-V characteristic of the ideal solar cell as shown in figure 1.11, where the curves are plotted with changed sign as is usually done in photovoltaics characterization measurements. The higher the series resistance, the lower is the short-circuit current. Similarly, the lower the shunt resistance, the lower the open-circuit voltage.

$R_s$  is induced by contact resistances, extraction barriers and other factors, while  $R_{sh}$  is caused by additional current paths or local shunts. In an ideal solar cell, the series resistance is small and the shunt resistance is infinite.

The following parameters describe the photovoltaic performances of a solar cell:

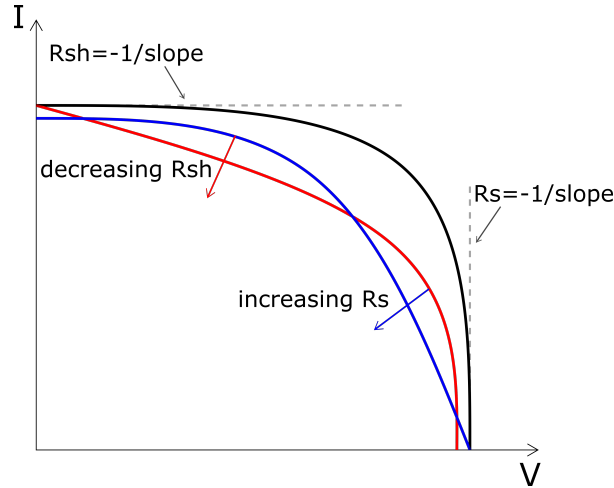


Figure 1.11: I-V characteristics of an ideal solar cell (in black), of a solar cell affected by low shunt resistance  $R_{sh}$  (in red) and affected by high series resistance  $R_s$  (blue). The shunt resistance is calculated from the inverse of the slope of the curve at  $I_{sc}$ , while the series resistance from the inverse of the slope at  $V_{oc}$ .

- $P_{max}$ , the maximum extractable power, is defined as the product between the maximum current and the maximum tension obtainable by the I-V characteristic:

$$P_{max} = I_{max} V_{max} (W) \quad (1.9)$$

- FF, the fill factor, defined as the ratio between  $P_{max}$  and the product between  $I_{sc}$  and  $V_{oc}$ :

$$FF = \frac{P_{max}}{I_{sc} V_{oc}} \times 100(\%) \quad (1.10)$$

Since the product  $I_{sc} V_{oc}$  is always larger than  $P_{max}$ , the fill factor is smaller than 100%.

- PCE, the power conversion efficiency, is defined as the ratio between  $P_{max}$  and the incident power  $P_{in}$ :

$$PCE = \frac{P_{max}}{P_{in}} \times 100(\%) \quad (1.11)$$

The power conversion efficiency express the ability of the solar cell to convert the incident power.

### Perovskite solar cell architectures

A typical perovskite solar cell structure is presented in figure 1.12, where the perovskite absorber layer is located between an electron and a hole transporting layers (ETL

and HTL).

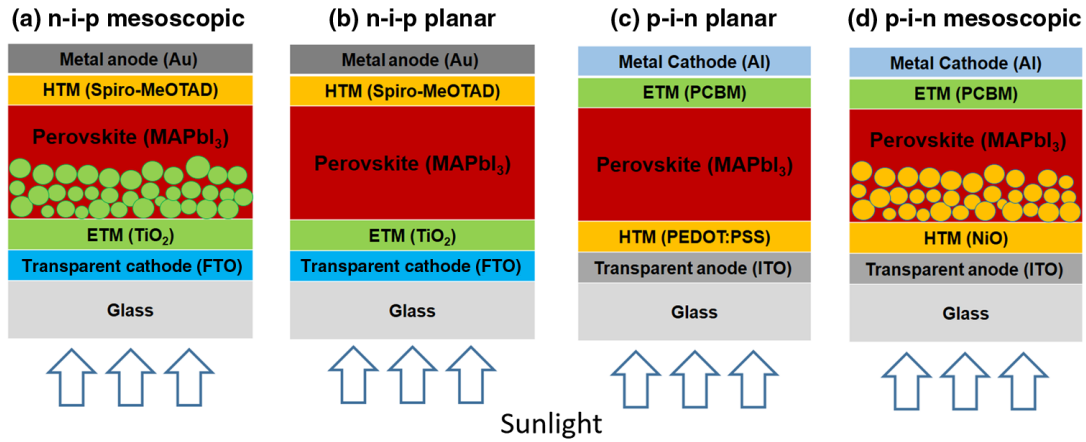


Figure 1.12: The four structures of solar cells: mesoscopic n-i-p, planar n-i-p, planar p-i-n and mesoscopic p-i-n. From [35].

The purpose of the hole transporting layer, also called electron blocking layer, is to promote the collection of holes with respect to electrons. The same is for the electron transporting/hole blocking layer but for the electrons. HTL and ETL are materials such that their valence and conduction bands allow for the separation of only one type of charge carrier with respect to the other, when in contact with the perovskites, as shown in figure 1.13. An additional scaffold layer can be inserted, between the compact ETL and the perovskite, made of  $\text{TiO}_2$ ; this structure is commonly referred to as "mesoscopic" or "mesoporous" n-i-p. If a scaffold layer with hole transporting properties is inserted between the compact HTL and the perovskite, the structure is referred to as mesoscopic p-i-n.

The structure without the scaffold layer is called "planar" and can be n-i-p or p-i-n, based on the sequence of the layers.

In the n-i-p configuration, the transparent-conductive layer (TCO), usually fluorine-doped or indium tin oxide, is in contact with the ETL, while in the inverted p-i-n configuration the TCO is in contact with the HTL. Finally, a metal electrode is placed on top. The two n-i-p and p-i-n planar structures, as well as the mesoporous structures, are reported in figure 1.12.

The HTL and ETL not only have to match with the energetic levels of the perovskite, but also need to provide a defect-free interface in order to minimize the recombination of photogenerated pairs.

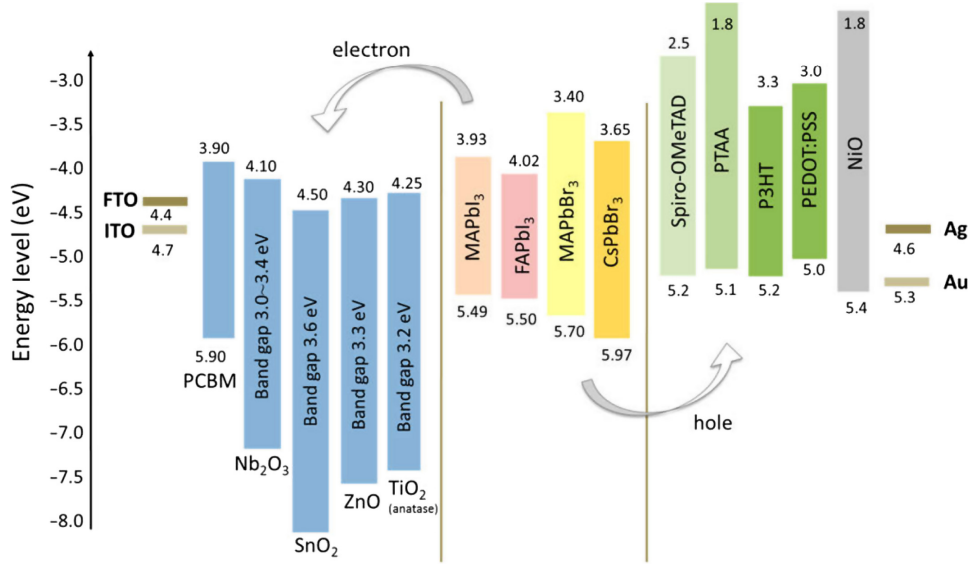


Figure 1.13: Comparison between the energetic levels of electron transporting materials, the perovskites, and hole transporting materials. ET layers have their energy bands such that electrons can flow from the conduction band of the perovskite to the conduction band of the ETL. While the flow of holes is energetically unfavored. The same is for the HT layers but for holes. From [37].

### 1.4.2 X-ray radiation photodetectors

Since the attenuation coefficient for X-ray photons is proportional to  $Z^4/E^3$  lead halide perovskites are suitable candidates for X-ray radiation detectors as they contain heavy atoms like Pb and I or Br. Moreover, thanks to their large bulk resistivity, perovskite-based photodetectors allow for achieving small dark current and noise. A high sensitivity, defined as the number of charges collected from the detector for unit of incident radiation energy, is also required.

With respect to solar cell devices, the perovskite absorbing layer must be thicker enough to stop the incident X-ray radiation; this is why lead halide perovskite single crystals have shown to perform better with respect to thin-film structures, also thanks to their higher degree of crystallinity.

As an example, Wei et al. [2] implement lead bromide perovskite single crystals in Au/MAPbBr<sub>3</sub>-SC/C<sub>60</sub>/BCP/Ag or Au structure (in figure 1.14) and achieved a X-ray sensitivity of  $80 \mu\text{C Gy}_{\text{air}}^{-1} \text{cm}^{-2}$  (derived from the slope of the 1.15 (c)). The high sensitivity is required as high doses are known to be harmful for the human body. The lowest detectable dose was  $0.5 \mu\text{C Gy}_{\text{air}}^{-1} \text{cm}^{-2}$  which is lower than required by regular medical diagnostics.

A remarkably high hardness to ionizing radiation is also observed; Yang et al. [38] found

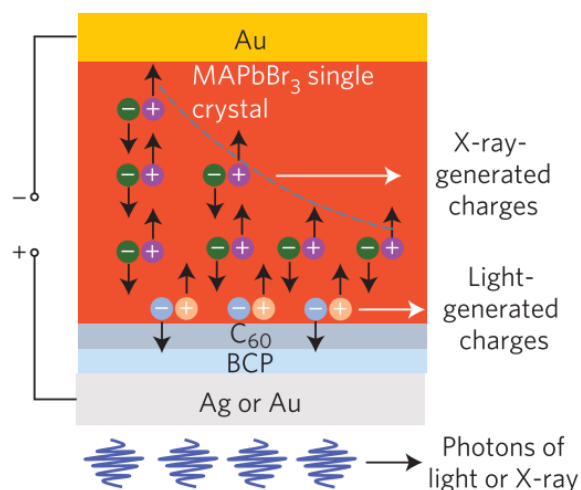


Figure 1.14: Single crystal radiation detector structure used in [2].

that the perovskite active layer retained 96.8% of its conversion initial efficiency after continuous irradiation with  $\gamma$ -ray and light for 1535h, with a total dose of 23 kGy. Lang et al. [39] reported a decrease of 20% of current density when irradiating the perovskite with a beam of 68 MeV protons. When the proton irradiation terminated, a self-healing process started and the current density recovered. The reason could be attributed to the high formation energy of deep defects, which is usually detrimental to the stability and to the performance of the device.

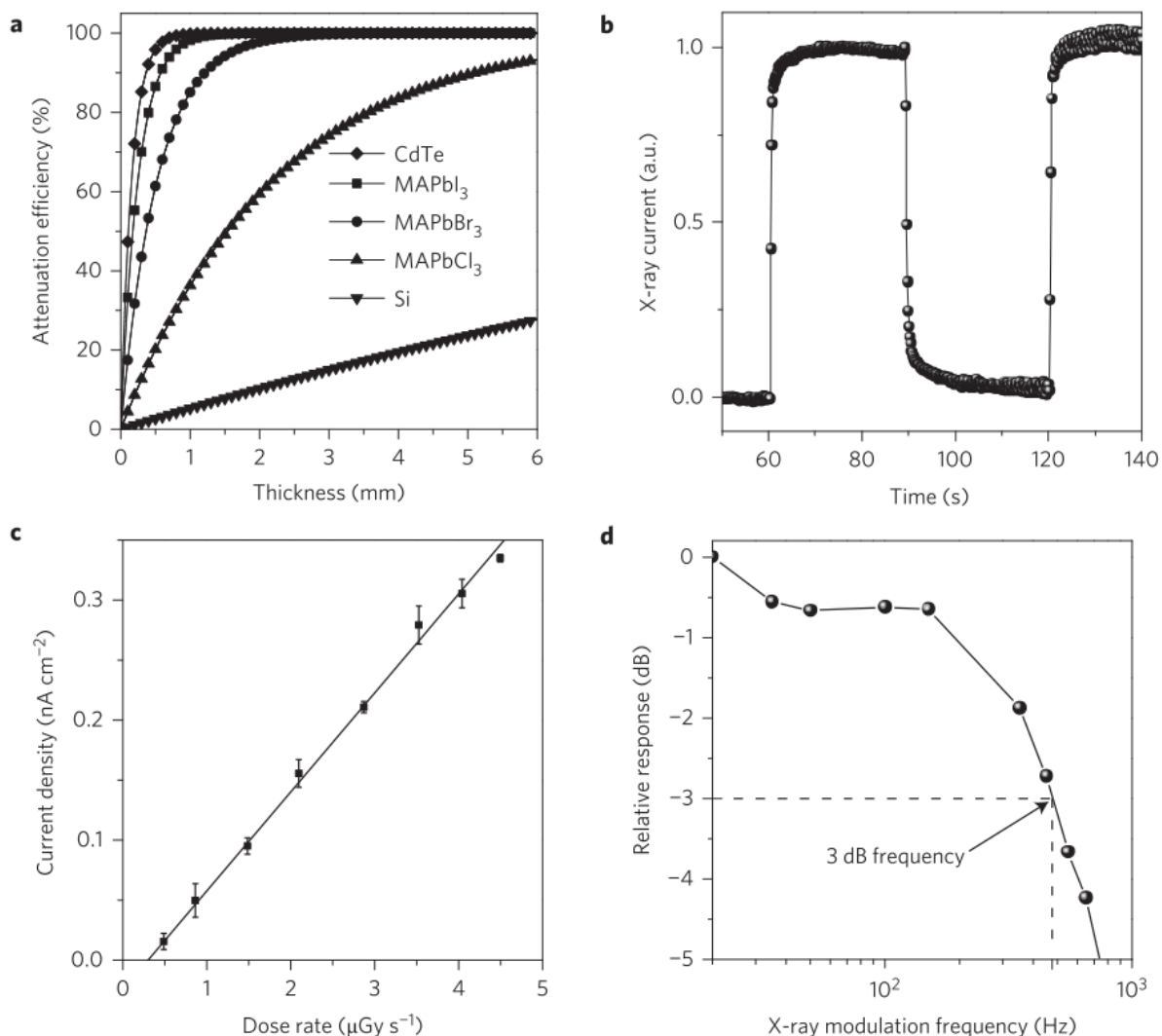


Figure 1.15: (a): comparison between the attenuation coefficient of CdTe, MAPbI<sub>3</sub>, MAPbBr<sub>3</sub>, MAPbCl<sub>3</sub> and Si to 50keV X-ray photons versus thickness. (b): MAPbBr<sub>3</sub> SC device response to X-ray by turning the X-ray source on and off. (c): X-ray generated photocurrent at various dose rates, down to the lowest detectable dose rate. (d): Normalized response as a function of input X-ray frequency showing the 3 dB cutoff frequency. From [2].

## 1.5 Defects, stability and health issues

The presence of defects, the degradation under moisture, oxygen and light can cause performance and stability issues and along with the toxicity of lead, all these factors can hinder perovskite devices from being commercialized.

A lot of effort has been done in order to both intrinsically improve or to stabilize the material.

In the following section, some of these problems will be addressed.

### 1.5.1 Defects

Hybrid halide perovskites are affected by defects which overall reduce the device performance. Two types of defects exist in perovskite: one-dimensional, like point defects and dislocations and two-dimensional defects, like grain boundaries. Defects can deform the crystal lattice and thus change the band structure. They can also introduce deep states within the gap that can act as recombination centers for holes and electrons.

The formation energy of these defects depends on the composition and on the growth conditions.

#### Point defects

Intrinsic point defects in halide perovskite can be interstitial (i), vacancy (V) or substitutional defects. It is generally found that these defects do not form deep states within the gap, but rather shallow levels. The formation of those defects and their position in the energy band in MAPbI<sub>3</sub> is reported in figure 1.16. Point defects like substitutional  $I_{MA}$ ,  $I_{Pb}$ ,  $Pb_I$  and interstitial  $Pb_i$  cause deep states, however their formation energy is high. While defects like  $I_i$  or  $MA_i$ , with relatively low formation energy, form shallow levels. This is the reason why perovskites are considered relatively defect tolerant and why sometimes a p-type or n-type behaviour is observed [40, 41]. A similar behaviour is found for the bromide perovskite [27]. The calculated energy levels of intrinsic point defects are reported in figure 1.17. Only  $Pb_i$ ,  $Pb_{Br}$ ,  $Br_{MA}$  and  $Br_{Pb}$  form deep levels within the gap. By calculating the formation energy in case of Br-rich/Pb-poor or neutral growing conditions, the Fermi level is such that the perovskite exhibits a p-type behaviour, while in Pb-rich/Br-poor condition the perovskite exhibits an intrinsic or slightly n-type behaviour.

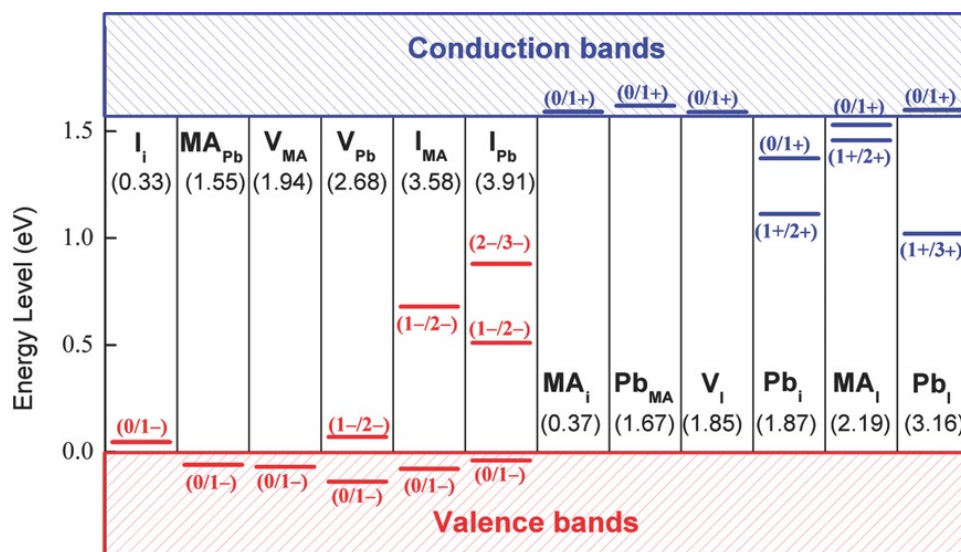


Figure 1.16: Energy levels of point defects of MAPbI<sub>3</sub> from [41].

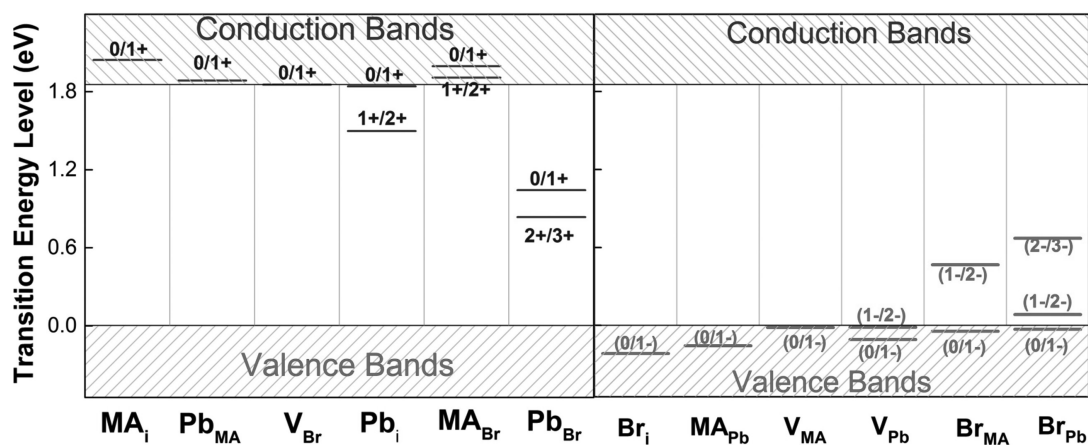


Figure 1.17: Energy levels of point defects in MAPbBr<sub>3</sub> from [27].

## Grain boundaries and surface defects

Grain boundaries are the most relevant 2D defects in film perovskites where most of the defects are located. Grain boundaries can provide pathways for water infiltration as well as charge accumulation.

Grain boundaries are particularly relevant for thin films and they can form non-radiative recombination centers and charges can accumulate; this forms potential barriers and consequently hinders the separation of the charge carriers.

Thanks to the absence of grain boundaries, perovskite single crystals have better optical and electronic properties with respect to their polycrystalline counterparts. However, the surface of a single crystal is affected as well by defects, caused by chemical impurities, dangling bonds, surface dislocations and undercoordinated atoms.

### 1.5.2 Stability

#### Humidity

Moisture is considered one of the most challenging issue [36] for hybrid halide perovskites. Due to the hygroscopic nature of the MA cation, the material absorbs easily water from the environment.

In presence of moisture, the methylammonium lead iodide perovskite undergoes the following degradation mechanisms:

- $CH_3NH_3PbI_3(s) \leftrightarrow PbI_2(s) + CH_3NH_3I(aq)$
- $CH_3NH_3I(aq) \leftrightarrow CH_3NH_2(aq) + HI(aq)$
- $4HI(aq) + O_2(g) \leftrightarrow 2I_2(s) + 2H_2O(l)$
- $4HI(aq) \leftrightarrow H_2(g) + I_2(s)$

The tendency of the perovskite to decompose is due to the hydrogen bonds between the organic and inorganic parts. Inserting a fraction of Br in  $MAPb(I_xBr_{1-x})$  solar cells improved their performance and stability; the reason is that by substituting the iodide with a smaller ion, the perovskite lattice shrinks, resulting in a more stable cubic perovskite due to a strengthening of the bonds between organic cation and lead halide [42].

Another way to stabilize the structure is by substitution of the A cation. It has been proved that the most stable perovskite structure is formed by alloying MA with the

larger FA and with Cs. Substituting a much larger organic cation in the A site transforming the 3D in a 2D perovskite also provides a superior moisture stability [36].

### Oxidation

Both perovskite layer and transport layers of solar cells can interact with oxygen, leading to oxidation-induced degradation that can be further enhanced by illumination. For what concerns the perovskite active layer, oxygen can diffuse through halide vacancies, which, as mentioned in the previous paragraph, have relatively low formation energy. Molecular oxygen can trap electrons in the conduction band and form charged and highly reactive superoxide  $O_2^-$  which can initiate an acid-base reaction with the acidic methylammonium site [36].

Tin-based halide perovskites have been shown to be more prone to oxidation than the lead perovskites, thus leading to a much less stable device [20].

For what concerns transport layers, ETL such as  $TiO_2$  catalyze the oxidative decomposition of the material in contact with it.

### Illumination

The behaviour of the perovskite upon illumination should be studied carefully for photovoltaic devices. Upon illumination, significant changes in the perovskite film can occur, such as halide segregation, ion migration and compositional degradation. For example, mixed halide perovskites such as  $MAPbBr_yI_{1-y}$  show a reversible phase segregation into  $Br^-$  and  $I^-$  under light exposure. This phenomenon is called Hoke effect.

Metal halide are known to photodecompose: upon photoexcitation, carriers can be trapped at defect sites which can oxidize iodide to iodine and reduce  $Pb_{2+}$  to  $Pb_0$ . Many reported the formation of metallic lead under x-ray irradiation [45, 46] and also under visible light [47].

### Reaction with electrodes

Metals, used as electrodes on top of perovskite, can react with the halogen and with the halide species produced under humidity, oxygen, light and heat.

For example, halide anions can diffuse from the perovskite to the metal electrode, corroding the metal and causing a halide deficiency in the perovskite. Metal in the contacts can form a redox couple with  $Pb^{2+}$  in perovskite films, accelerating the loss of halide

species and forming  $Pb^0$  [44]. Metal diffuses under the activation of heat and or light into the perovskite active layer, forming insulating metal halide species or defects states at the interface or in the bulk [36].

### 1.5.3 Health issues

The lead halide perovskite uses heavy metal ions such as lead that can impact on health and give rise to environmental issues. Alternative to lead such as tin are being studied. However, tin-based perovskites show lower stability due to the oxidation of tin, from  $Sn^{2+}$  to  $Sn^{4+}$  [20].

Moreover, the solvents used during the fabrication processes, such as dimethylformamide (DMF) and dimethylsulfoxide (DMSO), are toxic for both humans and environment.

# Chapter 2

## Experimental methods

The following chapter describes the preparation of the samples and the methods that have been used to characterize them.

The first part involves the fabrication of MAPbI<sub>3</sub> solar cells, which have been produced at the University of Konstanz (Germany) under the supervision of the PhD student Vaidvile Ulbikaite. The methods which has been used for the MAPbBr<sub>3</sub> single crystals, grown by the PhD student Giovanni Armaroli at the University of Bologna, are described as well.

The second part presents the experimental setup used to extract the photovoltaic parameters of the MAPbI<sub>3</sub> solar cells, and the characterization methods that have been employed to test the radiation hardness of the MAPbBr<sub>3</sub> single crystals under X-rays; in this regard, the working principle of surface photovoltage and photocurrent spectroscopy, along with the X-ray tube setup have been described.

### 2.1 Sample growth

The MAPbI<sub>3</sub> solar cell's layers have been deposited with spin-coating, which is one of the most common technique to deposit solutions. With the aid of a pipette, a certain amount of the solution is dropped on the substrate; the spin-coater rotates while the solution spreads over the substrate and the solvent evaporates. The spin-coating is a relatively easy and fast procedure; however, extra attention in choosing the right amount of solution, the type of solvent, and the setting parameters must be payed to obtain a uniform thin film.

The MAPbBr<sub>3</sub> single crystals have been grown with the seed-assisted inverse temperature crystallization (ITC) procedure, described in reference [48], which allows to get

reproducible and high crystalline samples.

### 2.1.1 MAPbI<sub>3</sub> solar cells

The device is a planar n-i-p structure where the Indium-Tin-Oxide (ITO) substrate is in contact with a compact TiO<sub>2</sub> electron transporting layer. The perovskite substrate is spin-coated on top of the TiO<sub>2</sub> in a two-step process where the PbI<sub>2</sub> layer is deposited firstly and the MAI layer secondly; the two-step deposition is a common procedure to obtain uniform films. Then the hole transporting layer, made of Spiro-OMeTAD with added Li-salt and Co-salt, is spin-coated on top of the perovskite layer. Finally, the silver contacts are evaporated on top. The structure of the solar cell is depicted schematically in figure 2.1.

A batch of 60 samples has been prepared and grouped with slightly different deposition characteristics, depending on how the contact with the ITO is created, on the type of additive for the HTL (Li or a combination of Li and Co salts) or on the spin-coating time for the HTL layer.

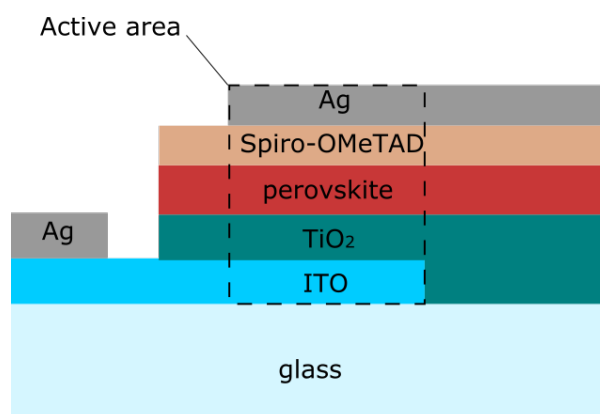


Figure 2.1: Scheme of the MAPbI<sub>3</sub> thin film solar cell in the n-i-p planar structure.

#### Fabrication procedure

The substrates are glasses covered with ITO with 15  $\Omega$  of sheet resistance. Each glass has been etched with zinc powder and hydrochloric acid in order to leave part of the ITO free, as shown in the right part of figure 2.1.

Then, the substrates have been cleaned in the ultrasonic bath firstly, and with the UV-ozone machine secondly, aiming to obtain clean glasses for the successive deposition. The TiO<sub>2</sub>, the Spiro-OMeTAD doped with Li and/or Co, the MAI and PbI<sub>2</sub> solutions have been prepared and stored inside of a glovebox in nitrogen atmosphere.

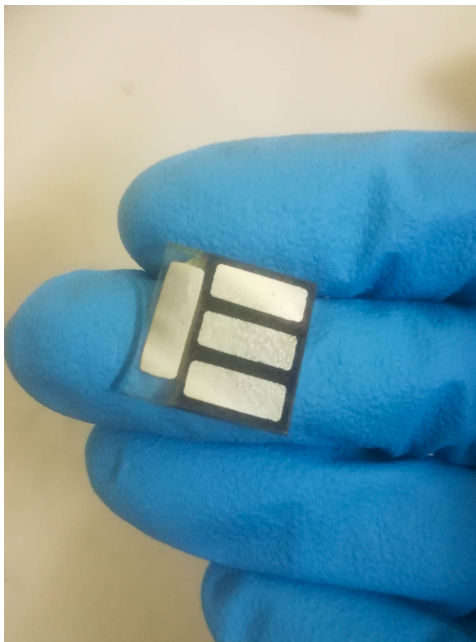


Figure 2.2: The final  $\text{MAPbI}_3$  solar cell.

Successively, the titania oxide solution has been spincoated and the sample are left to dry on a hotplate for an annealing procedure. The  $\text{PbI}_2$ , the MAI and the Spiro-OMeTAD solutions has been spincoated in controlled nitrogen atmosphere in order to reduce as much as possible the degradation of the perovskite layer.

Before the evaporation of the silver contacts, part of HTL and of the perovskite substrates has been removed in order to separate the ITO, as illustrated in figure 2.1.

Three contacts have been evaporated on HTL layer as top contacts and one contact on ITO layer as bottom contact. First a thin layer of tungsten oxide and then the layer of silver have been evaporated, to obtain a final thickness for the contacts of about 100 nm. The completed device is reported in figure 2.2.

### 2.1.2 $\text{MAPbBr}_3$ single crystals

The  $\text{MAPbBr}_3$  single crystals have been grown with the seed-assisted inverse temperature crystallization (ITC) method, as described in reference [48], based on the inverse solubility of the perovskites in specific solvents.

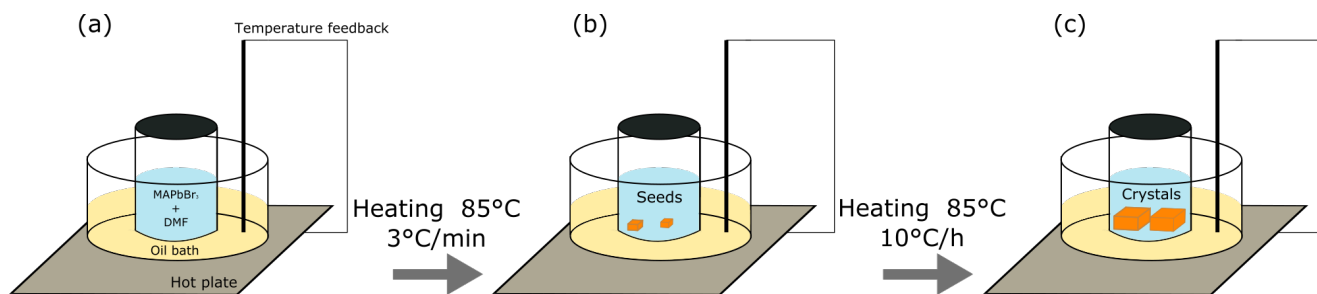


Figure 2.3: (a): the solution is heated from room temperature to 85°C. (b): the seeds grow by spontaneous nucleation. (c): the crystals grow around the seeds.

### Single crystal growth

The solution is prepared by dissolving MABr and PbBr<sub>2</sub> precursors in 1:1 molar ratio in DMF, to obtain 1 M solution of MAPbBr<sub>3</sub>. The solution is stirred at room temperature for 3 hours and filtered in a closed vial.

In order to obtain the seeds, the solution is heated up on a hotplate from room temperature to 85°C at 3°C/min rate. This is a relatively rapid temperature ramp which leads to the spontaneous nucleation and to the formation of many small crystals (steps (a) and (b) of figure 2.3). Then the crystal seeds are recovered from the vial.

A new 1 M solution of MAPbBr<sub>3</sub> is then heated up to 55°C at 3°C/min rate. At 55°C, one or more seeds are immersed in the solution, heated up rapidly to 65°C and then to 85°C at 10°C/h. This way the crystal nucleates heterogeneously around the seed in 2-3 hours (steps (b)-(c) of figure 2.3).

The resulting crystals are cubic-shaped, reflecting the cubic symmetry of MAPbBr<sub>3</sub> single crystals, with approximately 5x5x2mm dimensions each as shown in figure 2.4.

### Metal contacts

In order to perform I-V characterization and photocurrent spectroscopy, a layer of chromium and then a thin layer of gold are evaporated to obtain two coplanar contacts on top of the surface. The evaporation procedure consists in placing the filaments of the selected metals (in this case, Cr and Au) on tungsten wires inside the evaporator chamber, where the air is pumped out by a vacuum system; when the pressure reaches  $\sim 10^{-6}$  mbar, the filaments are heated up by gradually increasing the current flowing through the tungsten wires. As the filament melts, the metal's atoms evaporate and deposit on the sample, which are fixed on a faced-down metallic plate.

After the evaporation has been completed, the crystals have been fixed to a glass substrate by means of copper tape and silver epoxy paste, as shown in figure 2.5. The silver

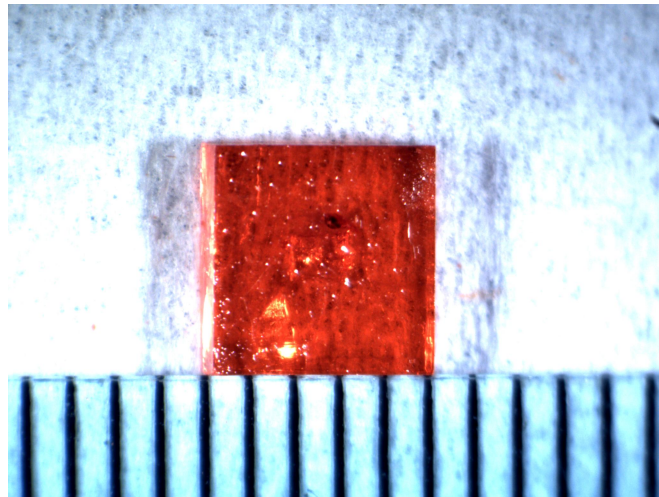


Figure 2.4: Top view of a MAPbBr<sub>3</sub> single crystal acquired with an optical microscope. At the center, the seed around which the crystal grew can be noticed.

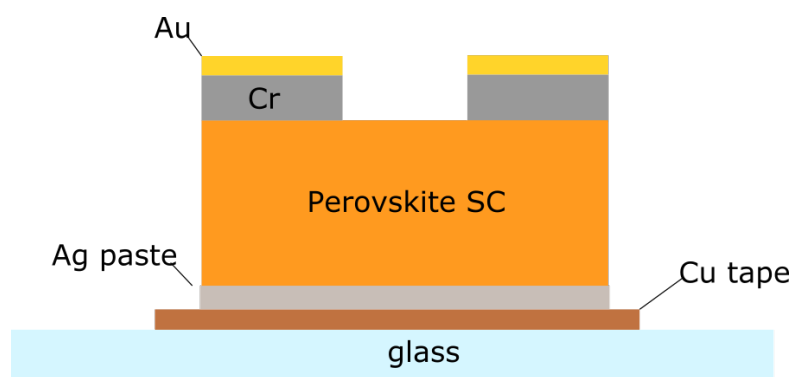


Figure 2.5: Side view of the MAPbBr<sub>3</sub> single crystals with Cu+Au top coplanar contact and Ag paste and Cu tape as back contact.

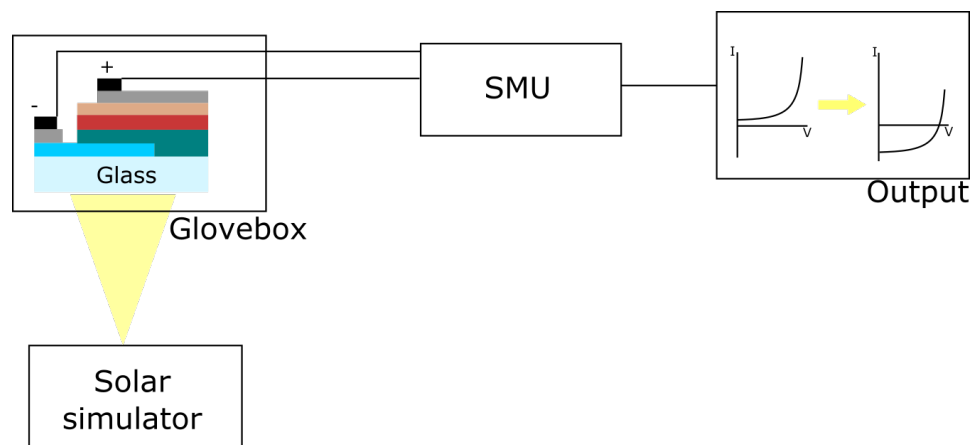


Figure 2.6: Setup for the characterization under dark and light condition of solar cells.

epoxy paste served also as back contact.

## 2.2 Characterization techniques

The thin film solar cells have been characterized via I-V measurement in dark and in light conditions, while surface photovoltage and photocurrent spectroscopies (SPS and PCS) have been used to optically characterize the single crystal samples, before and after X-rays exposure.

The SPS is a non destructive spectroscopy method that is usually performed in order to determine the semiconductor band gap, the type of semiconductor and defects states.

The PCS is a widely used optoelectronic technique to study the absorption of light and the transport of the photogenerated carriers.

### 2.2.1 Photovoltaic characterization

The setup used to measure the I-V curve of a solar cell in dark and under illumination is reported in figure 2.6;

the sample is placed inside a glovebox, filled with nitrogen atmosphere. A voltage sweep is applied and the current output is measured through a source measurement unit (SMU). In order to measure the output current under light condition, the sample is illuminated through the ITO-covered glass. The light source simulates the emission of the sun; a Xenon lamp reproduces the spectral irradiance of the sun at a standard Air Mass coefficient (AM) equal to 1.5, where the AM is defined as the inverse of the cosine

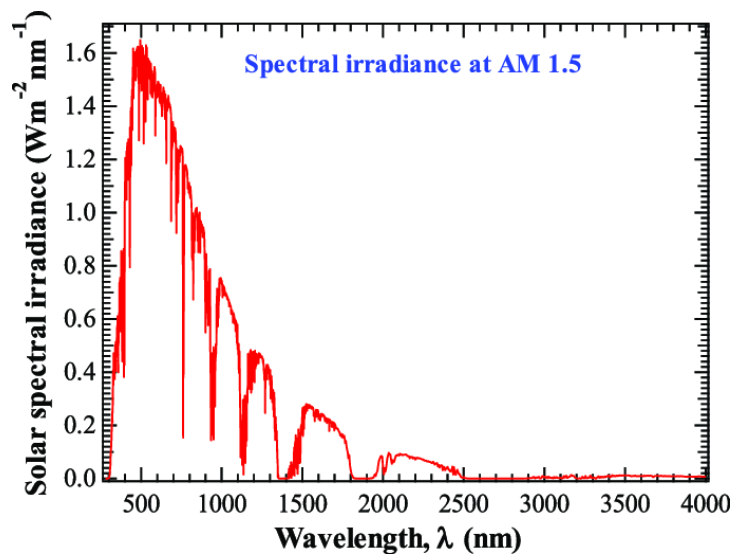


Figure 2.7: Spectral irradiance at AM=1.5 of the sun.

of the angle between the sun and the zenith. The simulated spectra of the sun at AM=1.5 is reported in figure 2.7. In standard condition, all solar cells are characterized by a input light intensity of  $100 \text{ mW/cm}^2$ .

### 2.2.2 Surface photovoltage spectroscopy

The SPS consists in measuring the surface photovoltage signal (SPV) induced by photogenerated carriers. The surface photovoltage involves a change in surface potential due to a generation and a subsequent redistribution of charges between the surface and the bulk [49].

#### Working principle of surface photovoltage

The termination of the periodic structure of a semiconductor at the free surface may form surface-localized states; these states include dangling bonds, surface reconstruction or relaxation, steps and kinks at the surface, impurity atoms absorbed at the surface [50].

Due to the presence of these surface states, the energy bands of a semiconductor are bent. This band bending causes a redistribution of charges between the bulk and the surface, thus forming a space charge region (SCR) near the surface with non-zero electric field. The potential difference between the bulk and the surface is called  $V_s$ .

Since at the surface there is typically a depletion of majority carriers with respect to the bulk, in a n-type semiconductor, the bands are bend upwards while in a p-type are bend

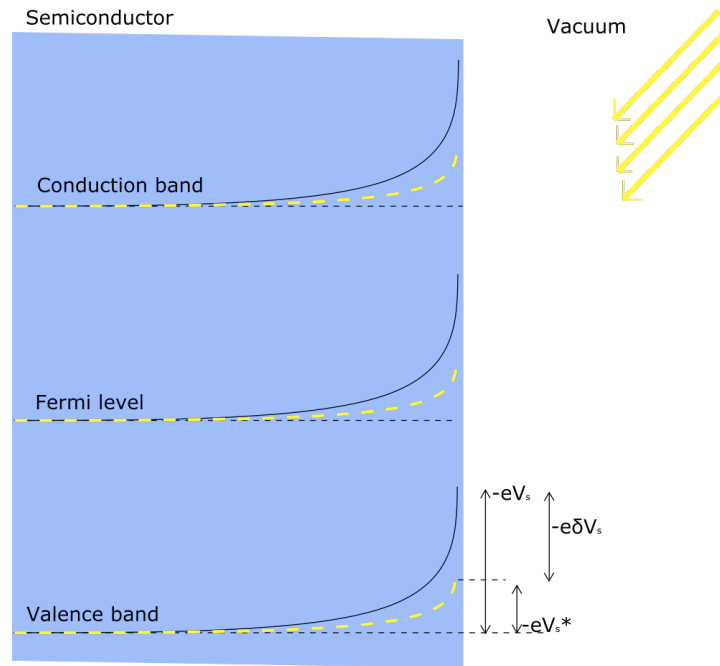


Figure 2.8: Bending of the energy states in dark ( $V_s$ , in solid black) and under illumination ( $V_s^*$ , in dashed yellow) for a n-type semiconductor. The flat dashed black line represents the bulk potential.

downwards. In the up-bending case, the  $V_s$  is positive while in the down-bending case the  $V_s$  is negative. The band bending in case of a n-type semiconductor is depicted in figure 2.8.

The excess carriers, generated by the impinging photons whose energy is higher than the band gap, are separated by the built-in electric field of the space charge region, so that one type of carrier moves towards the surface, while the other towards the bulk, as illustrated in figure (a) of 2.9. This exchange of charges between surface and bulk induces changes in the electric potential at the surface; in case of upward bending, holes are attracted at the surface, while electrons are repelled from it, thus resulting in a decrease of the band bending. In case of downward bending, electrons move towards the surface while holes towards the bulk, causing a decrease of bending in this case, too. The change of voltage induced at the surface by light with respect to the dark is reported in figure, for n-type 2.8.  $\delta V_s$  indicates the difference between the surface voltage in dark and in light. In figure 2.10 is illustrated the change in voltage for a n-type and a p-type semiconductor.

If the incident energy is lower than the band gap energy, the light can induce transitions between surface states, which lie within the gap, and the continuum states. In case of surface states-conduction band transitions, reported in figure (b) of figure 2.9, the elec-

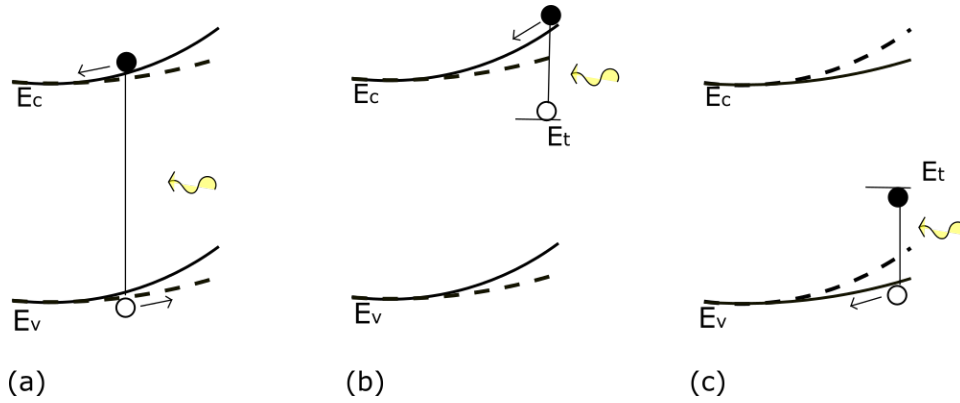


Figure 2.9: Mechanisms of generation and redistribution of charges in a n-type semiconductor. The solid and dashed lines indicate the energy bands before and after illumination, respectively. (a): Generation and redistribution between valence band and conduction band, (b): between surface trap state and conduction band, (c): between surface trap state and valence band.

tron is repelled away from the surface, causing a decrease of the band bending while the hole stays in the surface state. However, in case of valence band-surface states transitions, the holes accumulates at the surface, causing an increase of the band bending while the electron stays in the surface state; in this case an increase of the band bending occurs.

### Applications of surface photovoltage

The surface photovoltage signal is proportional to the absorption coefficient [51], according to:

$$SPV(\hbar\omega) \propto \frac{\alpha(\hbar\omega)}{\hbar\omega} \quad (2.1)$$

The SPV spectra can be used to determine the characteristic features of absorption, like the band gap or the exciton's binding energy. Usually, in order to determine the absorption coefficient a measure of both the transmission and the reflection coefficient are combined to extract the absorbance and then the absorption coefficient; this procedure has been used to calculate the absorption coefficient of MAPbBr<sub>3</sub> single crystals [52]. Rather, by means of equation 2.1, SPS allows to determine the absorption coefficient with a single measurement; however, the SPS, especially for energies below the band gap, is much more surface-sensitive with respect to the transmission spectroscopy.

SPS can be also used to determine whether the semiconductor is n-type or p-type. In both cases, photons with energy  $\hbar\omega > E_g$  decrease the band bending and the difference in signal will be positive for n-type semiconductors while negative for p-type semicon-

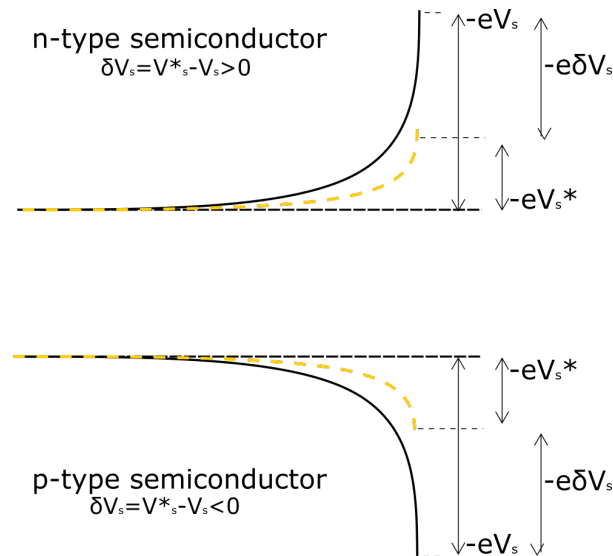


Figure 2.10: Band bending in case of dark (black lines) and light (yellow-dashed lines) for n-type or p-type semiconductors. The black dashed lines represents the bulk potential.

ductors, as illustrated in figure 2.10.

### Experimental setup for surface photovoltage spectroscopy

The surface photovoltage spectra are acquired in the metal - insulator - semiconductor (MIS) operation mode; the transparent electrode, a glass coated with indium-tin-oxide (ITO) is placed in "soft contact" with the semiconductor surface, as described in [51]. The surface of the ITO and the semiconductor form a parallel plate capacitor while the air in the middle acts as insulating layer. As illustrated in figure 2.11, the sample is mounted on a metal stage which can move in the x-y-z direction, in order to place the surface of the crystal parallel to the ITO coated glass. The beam of a Xenon lamp is first chopped at 20 Hz frequency and then sent to the monochromator. The potential voltage between the ITO and the back contact of the sample, generated by the accumulation of charges, is measured by connecting a 1 G $\Omega$  resistance in parallel with an amplifier, whose output is sent to the Lock-in Amplifier. The Lock-in filters out all the frequencies except for the 20 Hz, allowing a clean acquisition of the signal. The collected data are then fed into a PC and read by a LabView software.

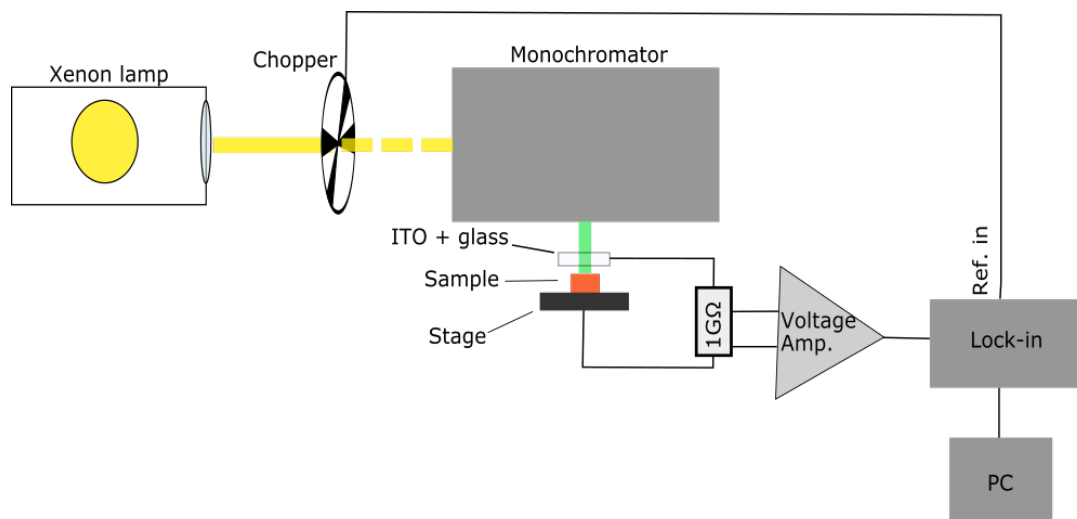


Figure 2.11: Block-diagram of the surface photovoltage apparatus.

### 2.2.3 Photocurrent spectroscopy

#### Working principles of photocurrent spectroscopy

When a semiconductor is irradiated with photons whose energy is higher than the energy gap, electrons absorb energy and are promoted to the conduction band. When these photoelectrons are created, simultaneously the conductivity inside the sample increases and the number of photons transmitted decreases.

The photocurrent spectroscopy technique consists in collecting this current at the electrodes as a function of the photon energy.

#### Applications of photocurrent

The photoconductivity is proportional to the absorption coefficient of the material [53]:

$$P \propto 1 - \exp(-d\alpha) \quad (2.2)$$

where  $d$  is the thickness of the sample. This relation is valid when the surface recombination is negligible compared with volume recombination. Photocurrent spectroscopy allows to obtain information about the energy gap, the degree of crystallinity and the distribution of shallow levels, which lead to an increase in conductivity for below-bandgap photon energies.

#### Experimental setup for photocurrent spectroscopy

The photocurrent setup is reported in figure 2.12. The sample is irradiated with a

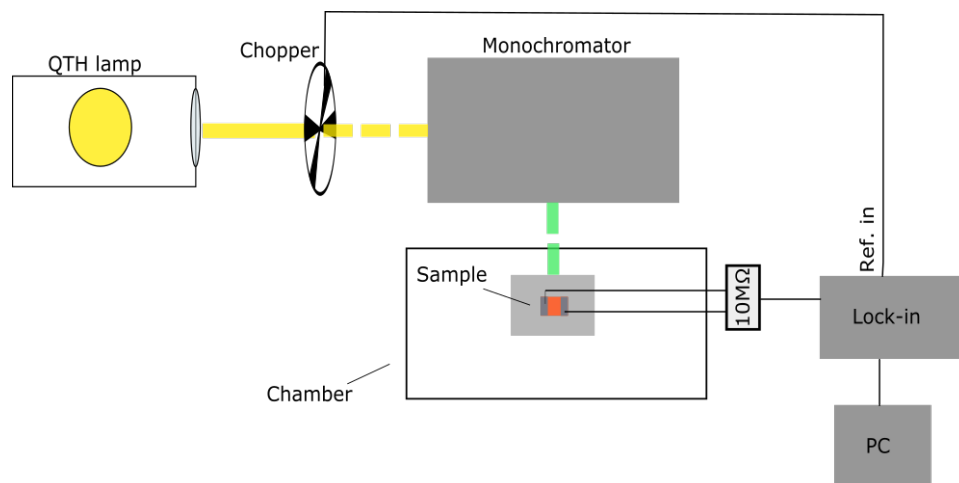


Figure 2.12: Block-diagram of the photocurrent spectroscopy.

QTH lamp that is first chopped at 20 Hz frequency and then sent to the monochromator. The monochromator sends one wavelength at a time in a chamber where the sample is kept in dark from ambient light. The photogenerated carriers are collected by two microprobes connected to the electrodes. The photocurrent is measured as a voltage drop across a 10 MΩ resistor. The output, as well as the frequency of the chopper are fed into the Lock-in amplifier, and then to the PC, where the software generates the photocurrent spectra.

## 2.2.4 X-ray irradiation setup

In order to test the radiation hardness of the MAPbBr<sub>3</sub> single crystals under X-ray photons, the samples are first irradiated with an X-ray beam in order to deposit a certain dose; In this paragraph, the concept of dose for ionizing radiation and the experimental setup used for the irradiation process will be introduced.

### Radiation dosimetry

The absorbed dose is a measure of the energy deposited in matter by the ionizing radiation.

The *gray* (Gy) is usually used as unit of measurement for the absorbed dose; it is defined as the absorption of 1 joule of radiation energy per kilogram of matter ( $\text{J} \cdot \text{kg}^{-1}$ ). The amount of energy absorbed by 1 kg of a substance strongly depends on the nature of the substance itself, on which the radiation is deposited. For this reason, in order to have a common reference, it is usual to use the  $\text{Gy}_{air}$ , which is defined as the energy (in J) absorbed by 1 kg of air. From now on, the amount of absorbed dose will be expressed

in  $Gy_{air}$  but indicated simply by Gy, in order to simplify the notation.

The *rad* is another used unit of the CGS system; it is defined as the dose causing 100 ergs of energy to be absorbed in one gram of matter ( $100 \text{ erg} \cdot \text{g}^{-1}$ ); in particular,  $1 \text{ rad} = 0.010 \text{ Gy}$ .

### Experimental setup

The experimental setup used for X-ray irradiation is depicted in figure 2.13. The X-ray tube is made of a tungsten cathode, which is heated up by a current in order to cause electrons to be emitted by thermoionic effect. Those electrons are then accelerated by a high potential difference towards the anode, made of tungsten. The impinging electrons excite the target core-shell electrons, which emit X-ray photons when going back to the equilibrium.

The emitted X-ray spectrum for the tungsten target is simulated in figure 2.14. Over the Bremsstrahlung continuum, caused by the decelerating electrons, the discrete peaks are characteristic of the energy of the tungsten core shell. From a previous calibration of the X-ray beam, it is known that the deposited dose rate on the sample, located at 9 cm from the tube, is  $75.82 \text{ mGy/s}$ .

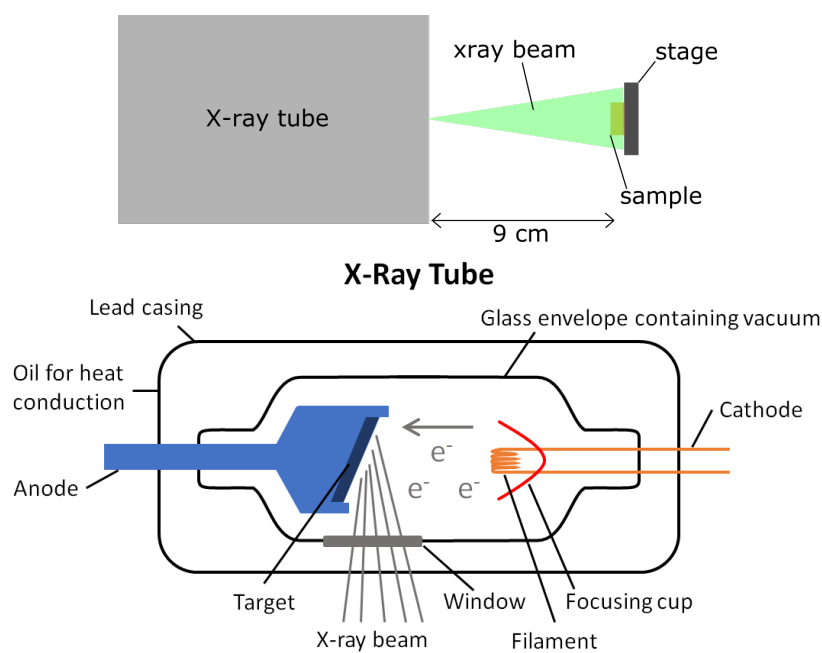


Figure 2.13: Setup used to deposit the radiation dose on the crystal, composed of a X-ray tube and a stage where the sample is located. The tungsten cathode is heated up by a  $500 \mu\text{A}$  current.

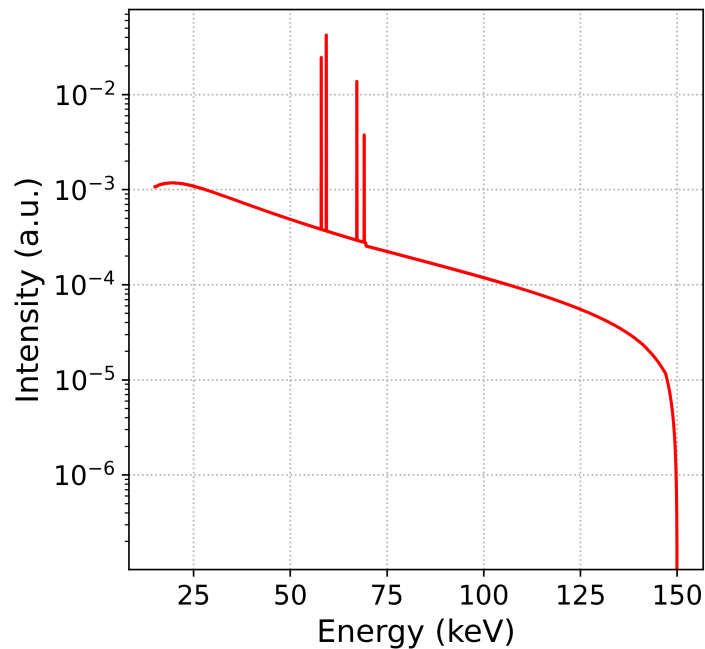


Figure 2.14: X-ray emitted spectrum from the tungsten target, where electrons are being accelerated by 150 kV. The spectrum is composed by the continuum emission and by the characteristic lines of the target.

# Chapter 3

## Optoelectronic characterization results

The following chapter is divided in three parts; the first contains a brief example of the photovoltaic characterization of one of the MAPbI<sub>3</sub> solar cell, fabricated as described in the previous chapter, through current-voltage measurement in dark and in light condition. The solar cells do not show the expected photovoltaic parameteres and further improvement of the devices has been hindered by the closure of the university due to the pandemic. The second part presents the characterization of the MAPbBr<sub>3</sub> single crystals as grown with SPS and PCS measurements; the third part is dedicated to the same SPS and PCS characterization after exposure to X-ray photons.

### 3.1 MAPbI<sub>3</sub> photovoltaic characterization

The MAPbI<sub>3</sub> solar cells have been characterized with I-V measurements in dark and in light and the main parameteres have been extracted from the output curve. The dark curve has been acquired by applying a voltage sweep from -0.1 and 1.2 V in 0.01 V steps. The results for one of the fabricated solar cells is reported in figure 3.1 (a). The solar cell shows a diode-like curve in dark. The current can be divided in three regions, respectively dominated by the shunt resistance, by the diode behaviour or by the series resistance in the low, in the middle and in the high voltage regions. As calculated from the dark I-V curve by the software, the shunt resistance and the series resistance are equal to  $R_{sh}=27366.8 \text{ } \Omega/\text{cm}^2$  and  $R_s=0.3 \text{ } \Omega/\text{cm}^2$ ; as explained in section 1.4.1, a high value for the shunt resistance is preferred, as it indicates that there are no current shunts; while the low series resistance shows that the contacts resistance and the

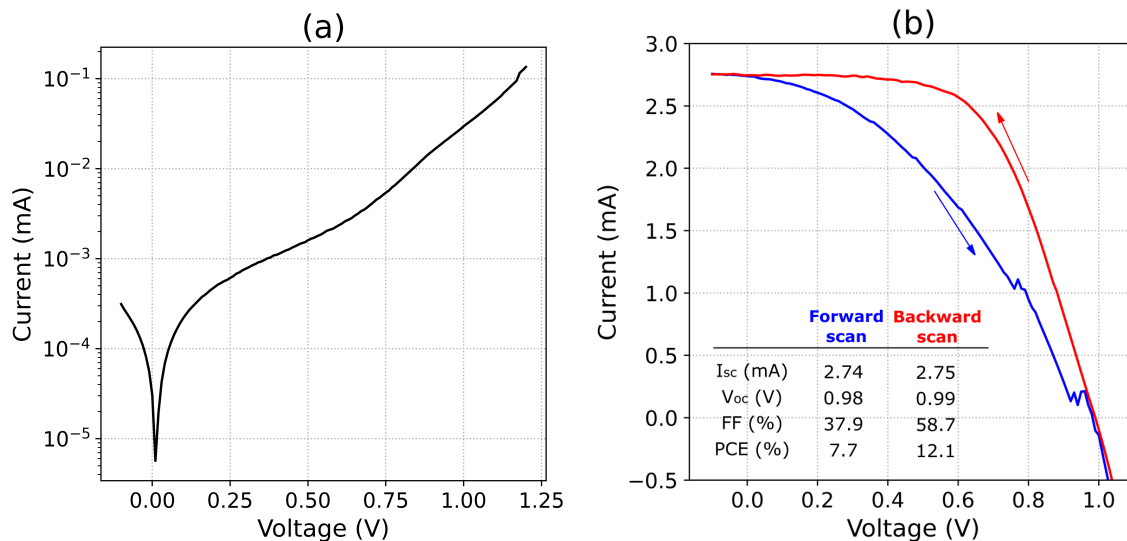


Figure 3.1: (a): diode behaviour of the MAPbI<sub>3</sub> solar cell in dark. (b): MAPbI<sub>3</sub> solar cell behaviour under illumination, in blue for the applied voltage scan in the forward direction, in red for the backward direction.

extraction barriers are low.

The light curves have been acquired by applying a voltage sweep between -0.1 and 1.2 V in 0.01 V steps; the solar cell has been illuminated through the transparent electrode with an intensity of 99.54 mW/cm<sup>2</sup>, scanning the voltage both in forward and backward direction. The results are plotted in figure 3.1 (b), from -0.1 to approximately 1.0 V, and with changed sign of the current, as for standard photovoltaic characterization.

The main parameters have been calculated by the software from the forward and from the backward curves and have been reported in the figure 3.1 (b). With respect to the forward direction, the backward scan presents a larger fill factor and a better power conversion efficiency given by a higher shunt resistance and a lower series resistance.

Differences between the forward and the backward scan in perovskite solar cells arise from hysteresis effects, by which the power output largely depends on the history of the device. Hysteresis in perovskites is connected to the migration of ions. Mobile ions can in fact accumulate near the interfaces, forming space charge layers. Those charge layers influence the charge extraction efficiency and give rise to different fill factors depending on the history of the applied voltage. In order to avoid hysteresis, the potential sweep should be slow enough to allow the ions to follow.

## 3.2 MAPbBr<sub>3</sub> optoelectronic characterization

Two single crystals, grown as described in the section 2.1 and named in the following 711 and 712 samples, have been characterized by surface photovoltage measurements; three SPV spectra have been acquired after 0, 72, 96 hours after the evaporation of the contacts, whose method is described in section 2.1, as well. The procedure is schematically depicted in figure 3.2.

The SPS results on a third not contacted sample, named here 613, are presented for

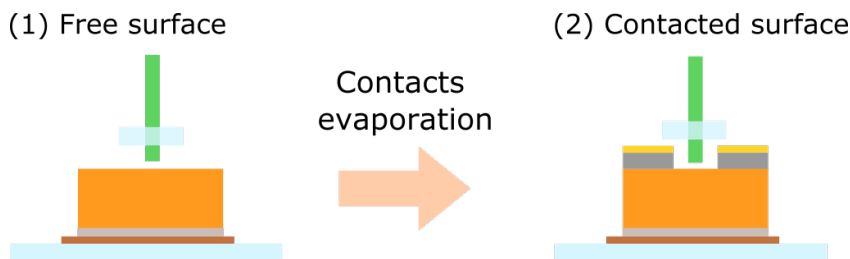


Figure 3.2: Surface photovoltage measurement before (1) and after (2) deposition of the contacts. In (2), the monochromated beam is focused on the free surface of the single crystal.

comparison. On the contacted 711 and 712 samples, I-V and PCS have been also performed.

### 3.2.1 Surface photovoltage spectroscopy

The SPV spectra are obtained by illuminating the surface with a photon beam, with wavelength ranging from 500 to 600 nm, in 2 nm steps. The frequency of the chopper has been set at 20 Hz and sent to the Lock-in Amplifier. The time constant  $\tau$  of the Lock-in's filter have been set to 1 s and the cut-off frequency to 12 dB/oct.

The acquired spectra are normalized to the Xenon lamp spectrum, which has been previously sampled with a pyroelectric sensor. With the aim to facilitate the visualization, all data have been normalized to 1, with the SPV signal at  $\lambda=500$  nm as normalization constant.

The results are reported in figure 3.3 (a) and (b) for the 711 and 712 samples.

As the main transitions of the SPV spectra are represented by slope changes, three features can be identified:

- The A-transition, due to the band-to-band absorption.
- The A\*-transition, due to the excitonic absorption.

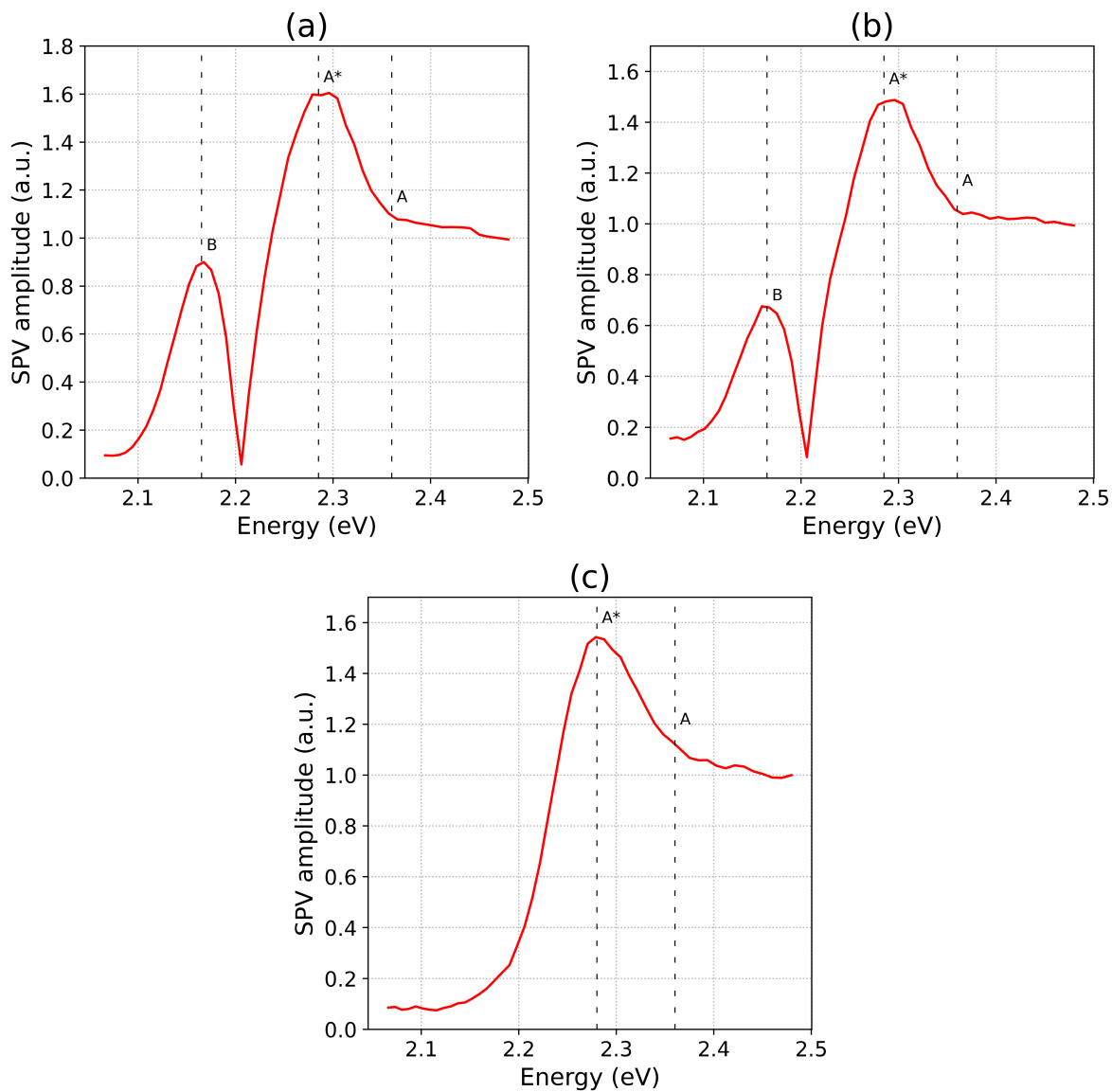


Figure 3.3: (a): SPV amplitude spectra of sample 711; (b): SPV amplitude spectra of sample 712, characterized as grown. The letter A indicates the band-to-band transition, B the below band-gap transition and A\* the excitonic feature. (c): SPV amplitude spectra of sample 613; the spectrum clearly exhibits the A and the A\* features, with no evidence of the B transition.

- The B-transition, due to a below band-gap absorption.

From 2.2 eV, up to higher energies, the SPV spectra exhibit the shape of a typical absorption in presence of excitons, as described in section 1.3.3: the signal is in fact characterized by a strong excitonic feature (A\*) followed by the continuum absorption of the band-to-band (A).

Despite being proportional to the absorption coefficient as indicated in expression 2.1, the SPV signal decreases in intensity in the higher end of the spectra; this phenomenon is often observed in presence of high surface recombination [54]. Moreover, the surface photovoltage requires both the photogeneration and the subsequent separation of the charges; as explained in section 2.2.2, the separation occurs thanks to the diffusion and to the build-in electric field. For these reasons, the surface photovoltage signal differs from the absorption coefficient.

The below band-gap B-transition is located at energies below 2.2 eV; however, this feature does not appear in every sample measured under SPS. As an example, the SPV amplitude spectra of the crystal 613 does not reveal any visible below band-gap peak (figure 3.3 (c)).

The SPV amplitude spectra after contacting the sample 711 are presented in figure 3.4 (a). Three spectra have been acquired after 0, 72 and 96 hours after the metal contacts have been evaporated on top of the single crystal surface. The height of the below band-gap peak (B-transition) of the 711 sample increases considerably, right after the evaporation of the top contacts; the amplitude becomes higher than the band-to-band transition of point A. The SPS have been repeated after 72h and 96h from the evaporation. A decrease in intensity of B peak is observed. After 96h, the B peak became lower than the initial amplitude.

A similar trend is observed for the 712 sample, where the sub-band gap peak increases after the evaporation and decreases in time. The behaviour of the B-peak height in SPV spectra is reported in figure 3.4 (b) as a function of time for sample 711, where all the points have been normalized to the height of the B-peak of the free surface. Right after the evaporation, the peak became about 3.5 times higher than the initial height. After 96h, the height decreased and became lower than the initial height.

### Analysis of the below band-gap peak

To further investigate the nature of B-transition, characterizing the energy region below the band-gap, the analysis of the SPV phase spectrum is performed: from the phase, it is possible to extract informations about the type of charge carriers involved in the

transition. The following hypothesis have been formulated accordingly to the method explained in reference [49].

The SPV amplitude and phase of the sample 711 is reported in figure 3.5 as a function of the photon energy. The phase of the SPV signal is characterized by two regions: during the B-transition, the phase shows positive values, around  $80^\circ$ , then drops to negative values, around  $-100^\circ$  in the A\*-transition region and maintains itself negative during the continuum A-transition. The negative phase in correspondence of the band-to-band transition A means that holes are being preferentially accumulated at the surface, while electrons are being separated toward the bulk. This phenomena is typical for a n-type semiconductor, as explained in the previous chapter.

The change from a negative to a positive phase means that an opposite process with respect the band-to-band is involved: electrons are being accumulated at the surface while holes towards the bulk. As a consequence, the SPV signal increases. This could mean that the below band gap peak is due to a surface state where electrons are being trapped, leading to an increase of the surface photovoltage instead of the usual decrease. This phenomenon is called "photovoltage inversion".

The phase of the SPV signal does not change after the evaporation; this means that the previous considerations about the type of charge carriers involved remain valid. Moreover, sample 712 shows the same behaviour of the phase.

The increase of the amplitude in figure 3.4 could be associated to an increment of the trap density and of the subsequent trapping of electrons by the same surface state.

Since the below bang gap peak often shows up in the SPV spectra right after the crystal growth, it could be related to an intrinsic defect such as  $MA_i$ ,  $Pb_{MA}$ ,  $V_{Br}$ , and  $MA_{Br}$ ; those defect, as described in section 1.5.1, have a low formation energy and result in shallow states that act as traps for electrons. Intrinsic defects mostly form due to an imbalanced stoichiometry (halide-poor or halide-rich conditions). Moreover, the surface is more prone to the formation of defects with respect to the bulk. Ambrosio et al. [55] investigated the trapping at the surface of the prototypical  $MAPbI_3$ , considering two different surface termination; the authors observed that the MAI-terminated surface is relatively defect tolerant. The  $PbI_2$ -terminated surface, on the contrary, favours the formation of Pb and I vacancies and I interstitial. One could expect a similar behaviour for the bromide-perovskite.

Extrinsic defects contribute as well to the formation of surface trap states depending on the enviromental conditions. Wang et al. [45] observed the degradation of  $MAPbBr_3$  single crystals under moisture and high vacuum; as suggested by the authors, the material degrades into  $CH_2$ ,  $HBr$ ,  $NH_3$  and  $PbBr_3$ ; where in particular,  $HBr$  and  $NH_3$  gases

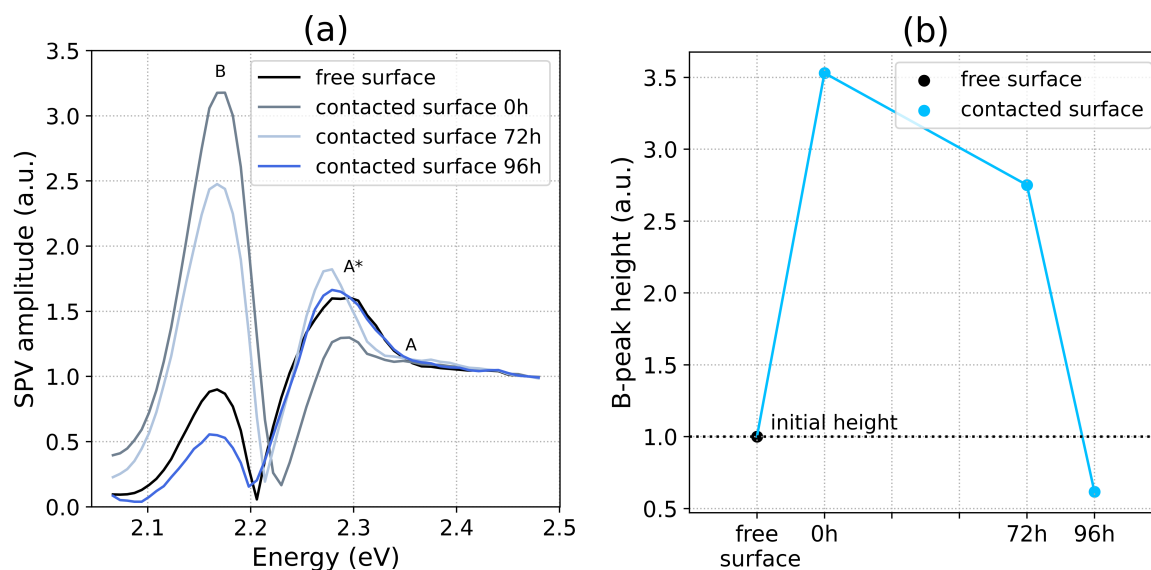


Figure 3.4: (a): SPV amplitude for the sample 711 before contacting the surface (black line) and after 0h, 72h and 96h from the contacts evaporation (grey and blu lines). (b): behaviour of the height of the B-transition with time with respect to the initial height, for the sample 711.

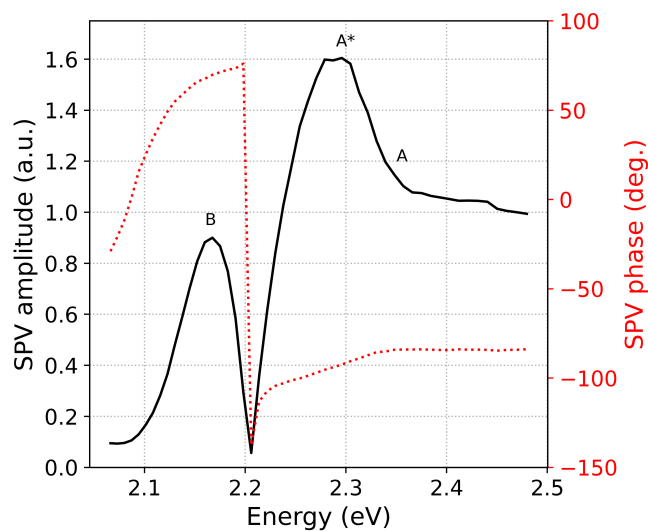


Figure 3.5: Amplitude (solid black line) and phase (dotted red line) of the surface photovoltage signal, before the evaporation of the contacts for the sample 711.

were released under vacuum. The analogous effect occurs in  $\text{MAPbI}_3$ , where the material degrades to  $\text{PbI}_2$ ; Deretzis et al. [56] observed the degradation of iodide perovskite into  $\text{PbI}_2$ , both in air and in vacuum. Moreover, from theoretical analysis, the authors suggested that the degradation could be associated to the formation of molecular vacancies, such as  $\text{HI}$  vacancies, localized at the surface. As described in section 1.5.2, also the presence of metal contacts could have played a role, for example by causing the loss of the bromide from the surface.

All summed up, the below band gap peak can be related to an intrinsic or extrinsic defect, which occurred owing to an involuntary unbalance during the growth process, or due to environmental conditions under which the crystal has been sottoposed, namely air, vacuum and metal contacts. In particular, the evaporation process, where the crystal has been subjected to high vacuum, to high temperature of the evaporated metals, and to the metals themselves could have enhanced the density of traps related to the surface defect and the consequent increase of electrons trapped by it.

The observed decrease in intensity after 72 and 96 hours from the deposition could be explained by a partial passivation; it was both experimentally observed by Zhang et al. [57] and Motti et al. [58] and calculated by First-principle by Zhou et al. [59] that oxygen is able to passivate defects in perovskite materials.

Some researches report the presence of defects states measured from surface photovoltage or from photocurrent measurements in perovskite materials [60, 61, 62]; however, further investigations on this below-band gap characteristic are required in order to understand its origin.

### **Analysis of the absorption**

Physical parameters as the energy gap and the binding energy of the exciton can be evaluated by fitting the experimental curves above 2.2 eV with the Elliott's absorption formula 1.6.

The SPV data have been multiplied by the energy (as required by the proportionality relation 2.1) and the fitting procedure has been applied in a reduced energy range, namely from 2.2 to 2.33 eV in order to exclude the B-transition and the higher energy tail which, as previously explained, is affected by surface recombination.

The energy gap, the exciton binding energy and the linewidth  $\Gamma$  are extracted from the fit. Two additional parameters have been added to the Elliott's formula in order to account for the possible different absorption baseline and the different scaling factor

between the model and the experimental data:

$$\alpha(\hbar\omega) \propto \alpha_{scaling} \frac{\mu_{cv}^2}{\hbar\omega} \left[ \sum_n \frac{2E_b}{n^3} g\left(\frac{\hbar\omega - E_g + E_b/n}{\Gamma}\right) + \int_{E_g}^{\infty} g\left(\frac{\hbar\omega - E}{\Gamma}\right) \frac{1}{1 - e^{-2\pi\sqrt{\frac{E_b}{E-E_g}}}} \frac{1}{1 - \frac{8\mu b}{\hbar^3}(E - E_g)} dE \right] + \alpha_{baseline} \quad (3.1)$$

The remaining parameters have been fixed to  $\mu_{cv}^2=1$  and the first exciton level only has been considered by putting  $n=1$ . The correction to the parabolicity of the bands,  $8\mu b/\hbar$ , has been set to  $0.091 \text{ eV}^{-1}$  as reported in reference [33].

The figure 3.6 simulates the excitonic (in red) and the continuum (in blue) contributions to the total absorption (in black), according to the formula 3.1, by setting  $E_g=2.3 \text{ eV}$ ,  $E_b=40 \text{ meV}$  and  $\Gamma=30 \text{ meV}$ . The figure 3.7 shows the SPV experimental curves and the

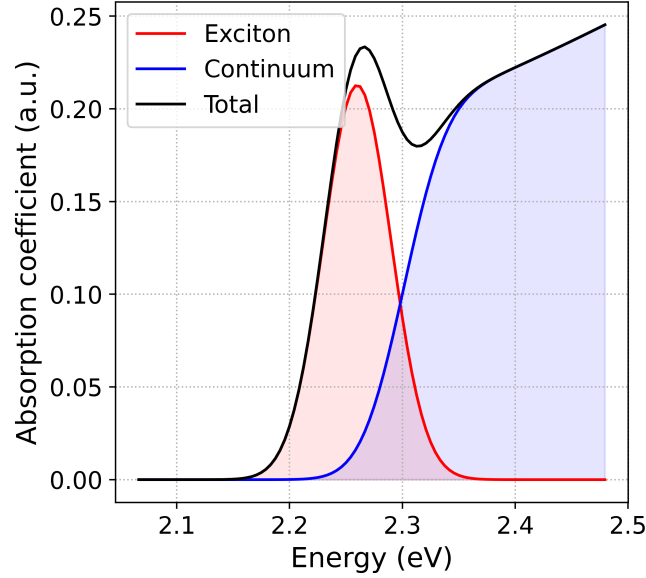


Figure 3.6: Simulation of the absorption in presence of excitons, according to the formula 3.1, with  $E_g=2.3 \text{ eV}$ ,  $E_b=40 \text{ meV}$  and  $\Gamma=30 \text{ meV}$ . The red curve represents the excitonic contribution, while the blue curve the continuum contribution; the sum is given by the black curve.

resulting fit for the samples 711, 712 and 613. The table 3.1 presents the parameters calculated by the fitting procedure. With respect to the experimental SPV curves, the fit with the absorption equation 3.1 differs in the higher energy region, affected by the surface recombination, and differs by the below band-gap peak, whose origin is still under analyses. Despite these two features, the best fit for the experimental curves yields to a comparable energy gap, exciton binding energy and linewidth, between the

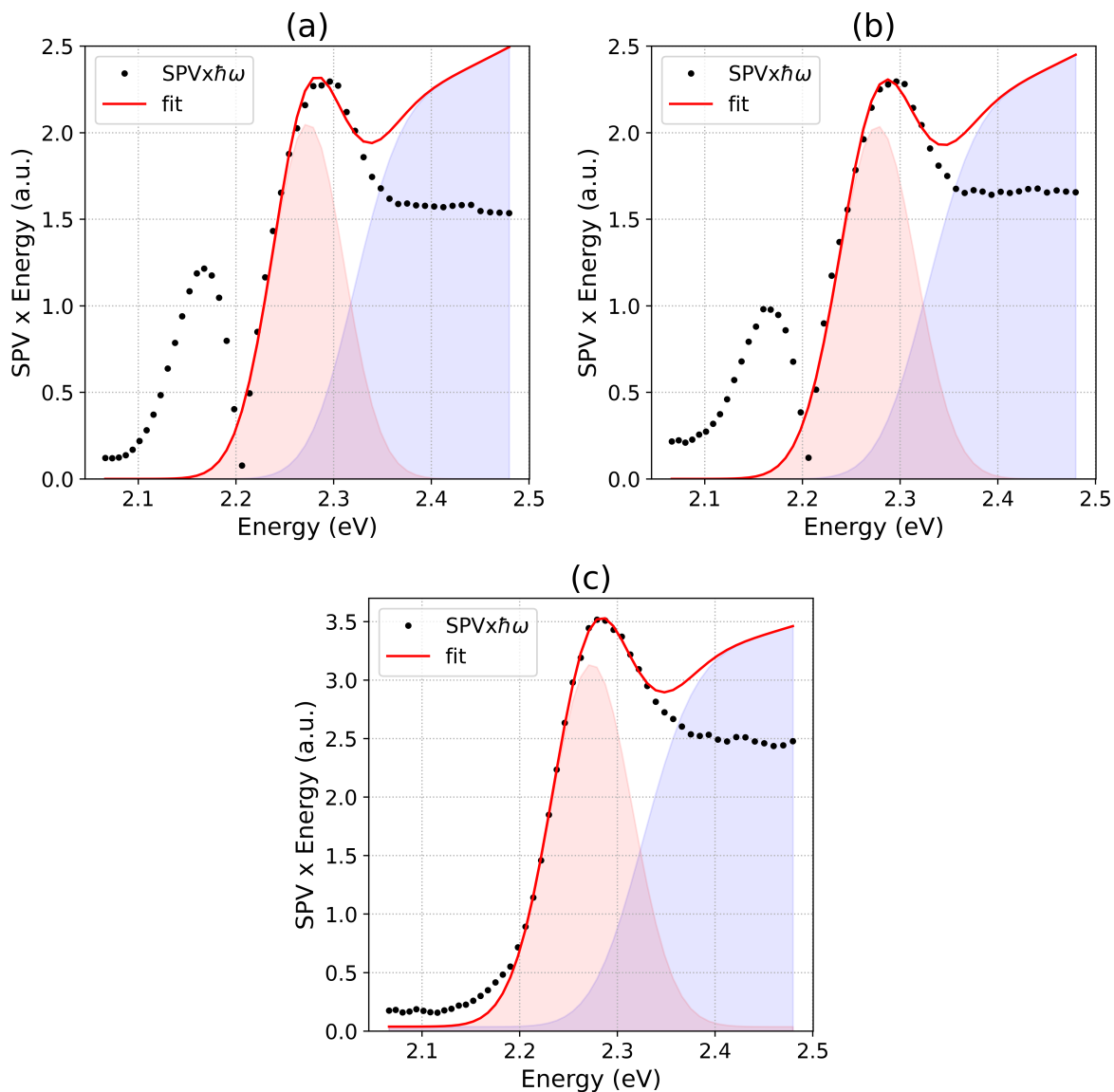


Figure 3.7: Experimental data (black dots) and fitted curves (solid red) for 711 in (a), 712 in (b) and 613 in (c). The fit procedure has been performed from 2.20 to 2.33 eV, while the fitted line has been graphically extended to the entire energy range. The shaded areas underneath the curves represents the excitonic contribution in red and the continuum contribution in blue.

Table 3.1: Parameters calculated from fitting of SPV data with Elliott's absorption formula.

Sample	$E_g$ (eV)	$E_b$ (meV)	$\Gamma$ (meV)
711	$2.32 \pm 0.01$	$45 \pm 7$	$37 \pm 3$
712	$2.32 \pm 0.01$	$48 \pm 8$	$39 \pm 3$
613	$2.326 \pm 0.003$	$52 \pm 2$	$42 \pm 1$

three samples, within the uncertainties.

### 3.2.2 Current - voltage characterization

The two samples 711 and 712 have been contacted, as explained in the previous chapter and electrically characterized by I-V measurements. A voltage sweep has been applied between the two coplanar contacts, as depicted schematically in figure 3.8, from -20 to +20 V in 1 V steps and with 1000 ms of delay between each step.

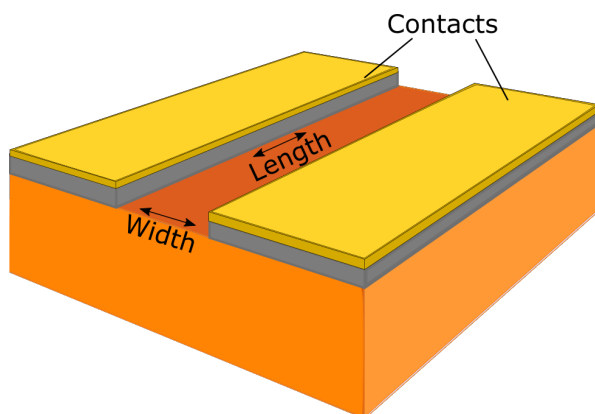


Figure 3.8: Side view of the MAPbBr<sub>3</sub> crystal with the two coplanar contacts.

The results of the I-V characterization are reported in figure 3.9 (a) for 711 and (b) for 712, with their relative fit. Both clearly display an ohmic behaviour. A linear fit of the experimental I-V curves has been performed in order to obtain a value for the resistance. In table 3.2, the sheet resistivities for the 711 and 712 samples are reported.

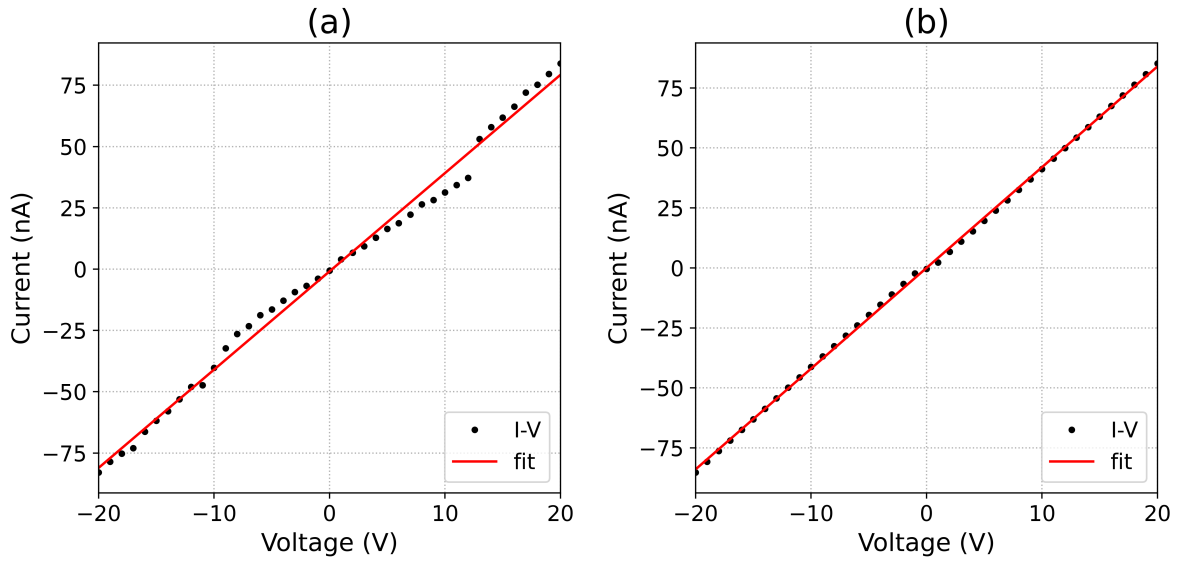


Figure 3.9: (a): I-V curve of 711 (black dots) and the relative fit (in red). (b): I-V curve of 712 and the relative fit. For both crystals the current is measured by applying a voltage difference between the two coplanar contacts.

Table 3.2: Sheet resistance calculated from resistance and from channel width and length.

Sample	Resistance (G $\Omega$ )	Channel length (mm)	Channel width (mm)	Sheet resistance (M $\Omega$ /square)
711	$0.249 \pm 0.003$	$5.0 \pm 0.1$	$1.2 \pm 0.1$	$60 \pm 5$
712	$0.2383 \pm 0.0008$	$5.0 \pm 0.1$	$1.1 \pm 0.1$	$52 \pm 5$

The resistance values reported in table have been extracted by the slope of the fit performed on the experimental I-V curves reported in figure 3.9. The sheet resistance is calculated from the width and the length of the channel between the two contacts, as depicted in figure 3.8.

### 3.2.3 Photocurrent spectroscopy

The two crystals 711 and 712 have been characterized by photocurrent spectroscopy. The PC spectra are obtained by illuminating the crystal with visible photons, with wavelength ranging from 500 to 600 nm in 1 nm steps. The frequency of the chopper have been set to 20 Hz; the time constant  $\tau$  of the lock-in amplifier filter to 1 s and the cut-off frequency to 12 dB/oct.

The samples have been measured under PCS after the last SPV measure (the one at 96h after evaporation). The samples have been illuminated at the top face and the current

has been collected from the two coplanar electrodes. With respect to the SPS, where the beam could be focused on the crystal surface only, here photons impinge on the two top contacts, as well.

The results are reported in figure 3.10 (a) and (b). All spectra are normalized to the QTH lamp spectrum, acquired with a pyroelectric sensor. All data have been normalized to 1, with the photocurrent signal at  $\lambda=500$  nm as normalization constant. Two distinct characteristics are visible in the photocurrent spectra, which, in analogy with the SPV spectra of figure 3.3, have been named A and B, indicating, respectively, the band-to-band transition and the below-band gap peak. The reason for this choice and the difference between the SPV and the PC spectra are further discussed below.

### 3.2.4 Comparison between Surface photovoltage and Photocurrent measurements

Figure 3.10 (c) and (d) compare the SPV (blue curve) and PC (red curve) signals, acquired one right after the other. With respect to SPV, the PC spectra differ in two ways; firstly, the transition B occurs at higher energy in the photocurrent spectra. Secondly, the transition A\*, related to the excitonic absorption, visible from the SPV, is not present in PC spectra.

The reasons for the discrepancy can be multiple: generally, the photocurrent spectroscopy technique does not only involve the photogeneration of charge carriers, but also their transport and collection at the electrodes; in addition, even if the current is collected between the two coplanar contacts (so the current is mainly flowing at the surface), PCS is still a bulk-sensitive technique with respect to SPS; lastly, the area illuminated by the photon beam in the photocurrent setup included also the metal contacts on the surface. For these reasons, even if SPS and PCS are both proportional to the absorption coefficient, two spectra acquired with these techniques do not always coincide. The calibration of both surface photovoltage and photocurrent monochromators has been verified to be the same and thus a different calibration has been excluded to be the origin of the shift between the two spectra. The shift in energy of the below-band gap peak could be attributed to the different mechanism of charge transport that involves the photocurrent. It is known that transport in perovskite materials involves not only electronic, but also ionic contribution; in particular, for the MAPbBr<sub>3</sub>, this would be caused by the Pb<sup>2+</sup> and Br<sup>-</sup> ions. Due to their heavier mass with respect to electrons, they can interact with electrons and also accumulate near the metal-perovskite inter-

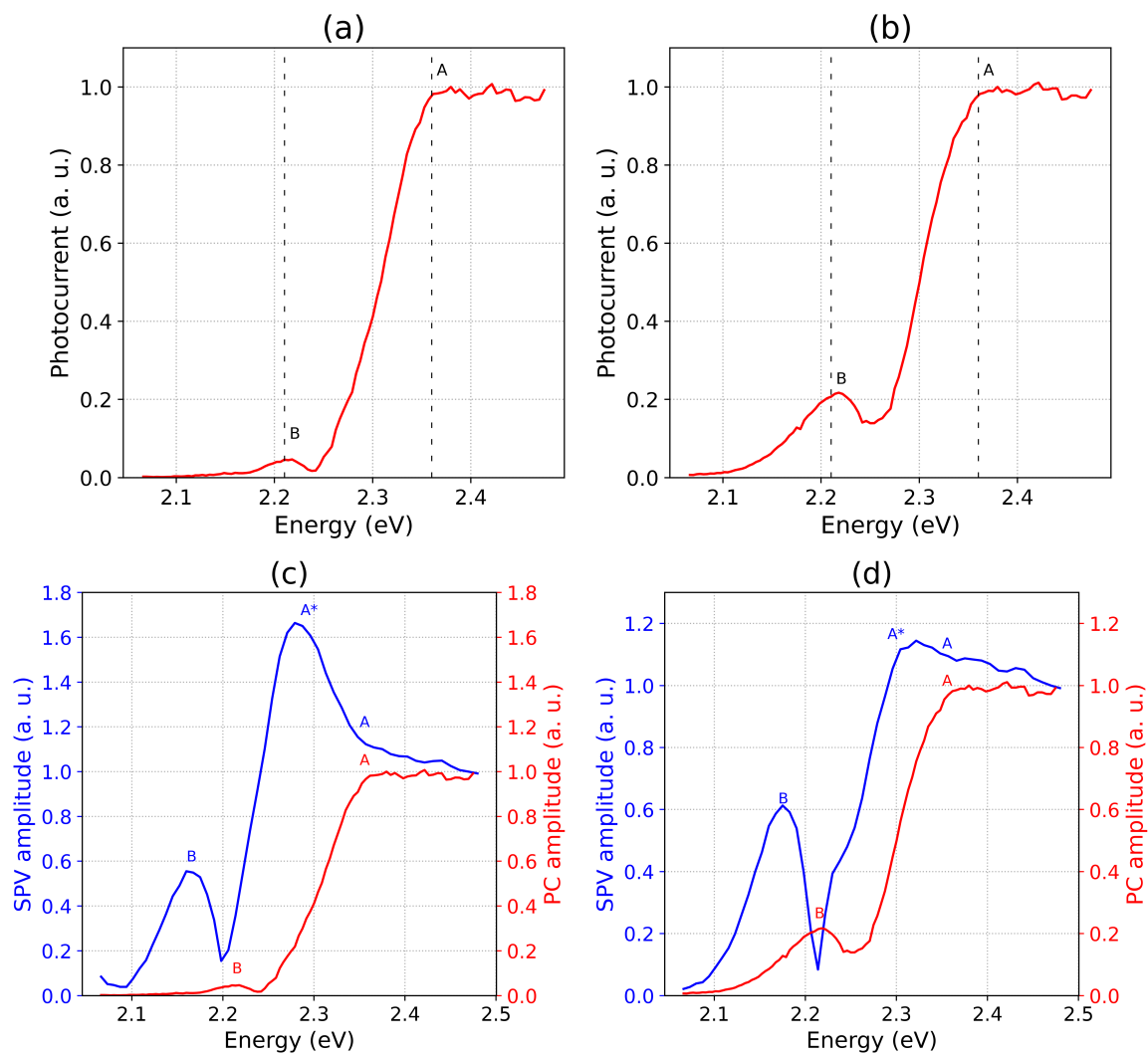


Figure 3.10: (a) PC amplitude spectra of sample 711. (b) PC amplitude spectra of sample 712. Comparison between SPS (in blue) and PCS (in red) of sample 711 (c) and 712 (d).

face, leading to a space-charge field near the electrodes. The fact that the photocurrent response could be dominated by a random and uncontrollable effect such as the ionic transport is suggested also by the plot of figure 3.18 (b), where the position of the below band gap peak is not fixed, but varies between the energies 2.17 - 2.21 eV. Moreover, the field produced by the accumulating ions could also be perceived by the charge carriers as a potential barrier that led to a decreased photocurrent signal. In this regard, Lafalce et al. [63] underline the important role of intrinsic ionic impurities such as Pb<sup>2+</sup> and Br<sup>-</sup> in controlling the photocurrent response. On the contrary, the accumulation of ions at the electrodes hardly affects the SPV spectra, since the charges are photogenerated and separated in small spot on the surface where the light beam is focused, while in the photocurrent spectra a much broader area of the crystal is illuminated, including the electrodes. Another reason that could justify the difference in position of the B-peak between photocurrent and surface photovoltage relies on the presence of the excitonic A\* transition in SPV with respect to the photocurrent. The SPV signal coming from A\* has higher amplitude and opposite phase with respect to the signal coming from B, as can be noticed from figure 3.5. This strong and opposite in phase signal could have hindered the signal of B, that consequently appears at lower energies.

The absence of peak A\* in the photocurrent spectra, reported in figures 3.10, could be justified again by the different transport mechanism involved in photocurrent and in surface photovoltage. The ionic species could have weakened the electrons' mobility, causing, in turn, a decreased collection efficiency of charges at the electrodes; this could be the reason for the lack of the absorption peak.

### 3.3 MAPbBr<sub>3</sub> X-ray hardness characterization

In order to assess the effects of X-ray irradiation, the two contacted samples, 711 and 712, have been measured with SPS and PCS. The measurement procedure consisted in irradiating the 711 sample with a 20Gy dose and measuring its surface photovoltage firstly and photocurrent spectrum secondly, according to the flow chart of figure 3.11; this sample is referred to as "irradiated". This procedure has been repeated until a total dose of 140Gy has been deposited.

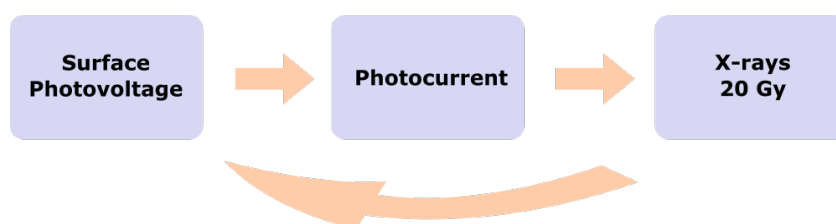


Figure 3.11: Scheme of the measurements for the X-rays radiation hardness tests for the 711 sample.

The 712 sample, instead, has been measured with SPS and PCS the day after, without exposure to X-rays; this sample is referred to as "control" and is compared with the irradiated one in order to discern the effects of X-ray photons. The recovery of the 711 sample have been also recorded by measuring its SPV and PC spectra after some hours from the deposition of the 140Gy X-ray dose, to see whether the changes in the spectra were reversible or not.

The 613 sample's results after X-ray exposure are reported as well; in this case, on the crystal, characterized with SPS only, has been deposited a total dose of 260Gy in 20Gy dose steps. The results for the related control sample, which has been measured the day after with SPS and without previous irradiation are reported as well.

### 3.3.1 Surface photovoltage spectroscopy

All data presented in this section have been acquired with the same setting parameters reported in section 3.2.1. Selected spectra of the 711 irradiated and of the 712 control samples are reported in figure 3.12 (a) and (b).

From the slope changes, 4 main features of the SPV spectra after irradiation have been

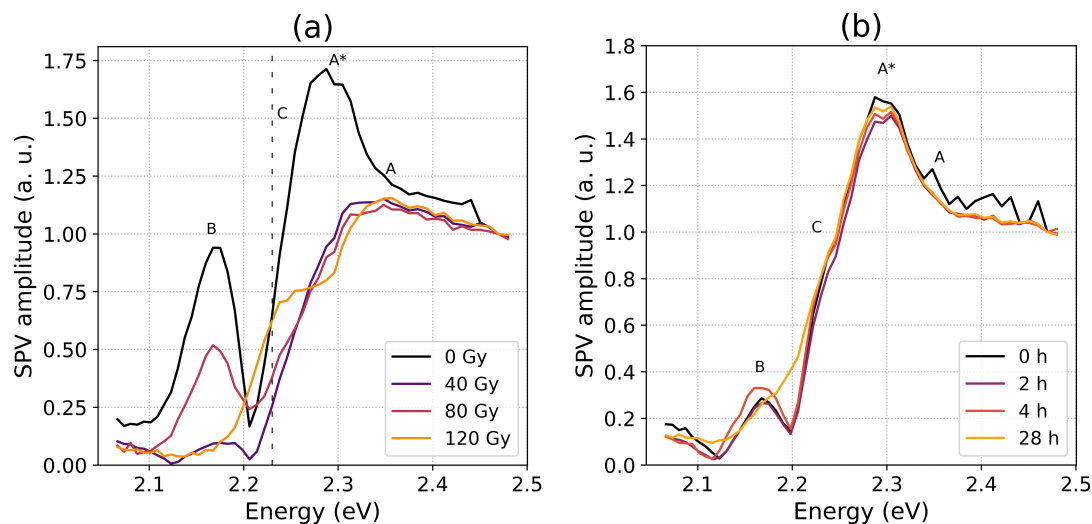


Figure 3.12: (a): SPV amplitude spectra of 711 irradiated sample after exposure to X-rays in 20Gy steps; selected spectra are reported, namely the ones at 0, 40, 80, and 120Gy doses. (b): SPV amplitude spectra of the control 712, measured every hour the day after; here the ones at 0, 2, 4 and 28 hours are presented.

identified:

- The A-transition, due to the band-to-band absorption.
- The A\*-transition, due to the excitonic absorption at 0Gy.
- The B-transition, due to the below band-gap absorption.
- The C-transition, a new peak that appears with the X-ray dose.

The 0Gy spectrum, the one acquired before the first 20Gy deposition, is characterized by the very same three features, A, A\* and B, described previously.

While the intensity of the B peak changes randomly from one deposition to the other, the excitonic feature, A\*, disappears and a new characteristic, named here with the letter C and located at around 2.23 eV shows up at 80Gy and increases with the deposited dose. The 712 control sample is characterized by a less prominent below band gap peak, while the excitonic absorption at point A\* does not change in time. The peak C appears as a

slightly visible and constant should instead of a clear peak like for 711. Over all, B, A\* and A transitions remains constant with time.

The figure 3.13 (a) presents the SPV amplitude spectra after irradiation of the 613 sample; the behaviour of the related control sample is presented in figure 3.13 (b). As

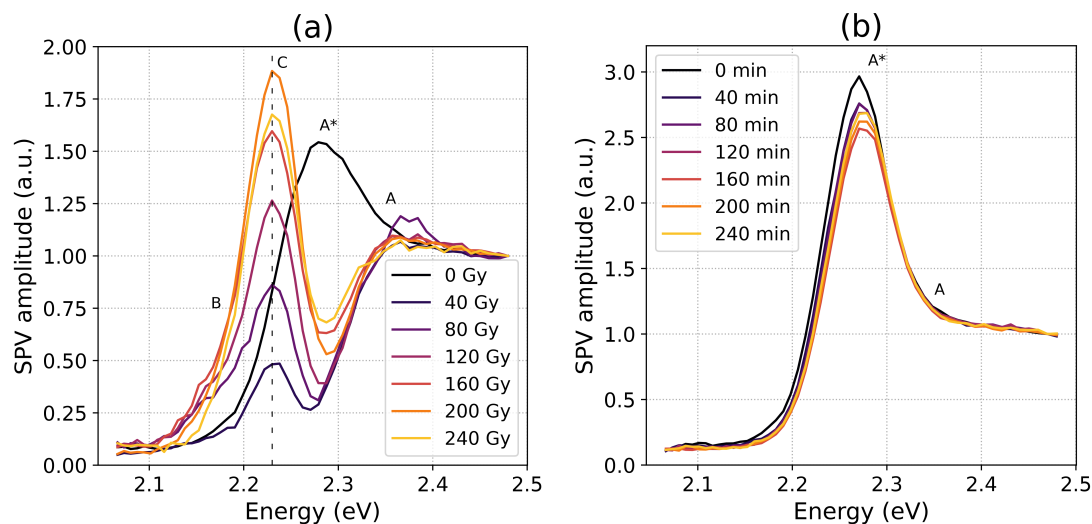


Figure 3.13: (a): SPV amplitude spectra of 613 irradiated sample after exposure to X-rays in 20Gy steps; selected spectra are reported, namely the ones at 0, 40, 80, 120, 160, 200, 240 Gy doses. (b): SPV amplitude spectra of the related control sample measured every 20 minutes the day after; here the ones at 0, 60, 80, 120, 160, 200, 250 minutes are presented.

described in section 3.2.1, the spectrum at 0Gy of the crystal 613 is characterized by the excitonic and continuum absorption (A\* and A), but not by the below-band gap transition at point B. Upon irradiation, the A\*-peak disappears and a new peak, located at point C, appears just after the first deposited dose; this new feature, visible in the 40Gy spectrum of figure 3.13 (a), is located at 2.23 eV. The higher the dose, the more intense the C-transition becomes.

Despite being located at the same photon energy and displaying the same increasing behaviour with doses of sample 711, the sample 613 presents a clearly distinct peak at 40Gy; this peak increases in intensity for sample 613, while it only appears as a shoulder, merged with the continuum absorption, for sample 711. The control sample, presented in figure 3.13 (b), maintains its SPV spectrum stable with time.

The recovery of the 711 sample has been measured after 15, 21 and 33 hours from the last deposited dose. The spectra in figure 3.14 shows a partial attenuation of the C-transition. Meanwhile, the B-transition decreases in intensity. The graph in figure 3.15 displays the behaviour of the height of the B-transition, for the 711 irradiated sample in

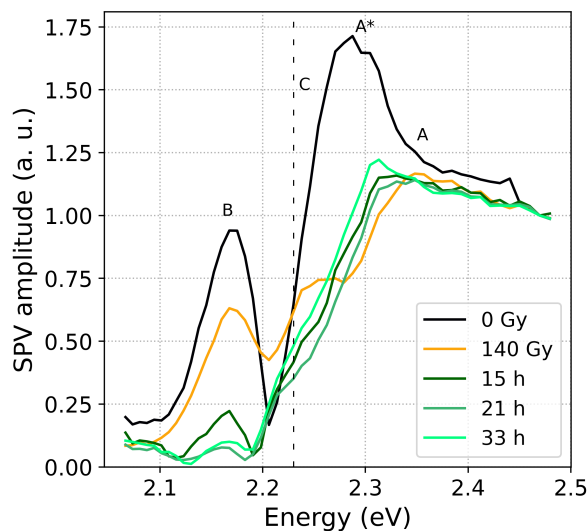


Figure 3.14: SPV amplitude spectra of the recovery of the 711 irradiated sample, measured after 15, 21 and 33 hours after the last deposition at 140Gy. The curves at 0Gy and 140Gy, in black and yellow respectively, are reported for comparison.

comparison with the 712 control sample; all values have been normalized to 1, with the initial height as the normalization constant. Except for the first decrease with respect to the initial height, the B-peak height of the control sample 712 is subjected to small changes, all around 40% from the initial value. On the contrary, the irradiated sample 711 shows a decrease of 60-70% with respect to the initial value and oscillates greatly with the deposited dose. As already indicated, the B feature is associated to a defect state located below the conduction band, whose intensity seems to be influenced by the X-ray irradiation.

### Analysis of the absorption

The curve at 0Gy and the curve at 200Gy of sample 613 have been fitted with the same procedure described in section 3.2.1; the sample 613 has been chosen over sample 711 thanks to the absence of the below band gap peak. Moreover, in view of the fact that the new characteristic appearing after irradiation in 613 is well deconvoluted from the continuum absorption, the fit results easier to perform.

The curve at higher doses, namely at 200Gy, has been considered under the hypothesis that, after the X-ray deposition, the exciton binding energy had increased, with respect to the curve at 0Gy. This assumption relies on the fact that the excitonic peak A\* visible at 0Gy, disappears right after the X-ray irradiation and a new peak C, at lower energies, appears. Moreover, measurements of photoluminescence (PL) performed at

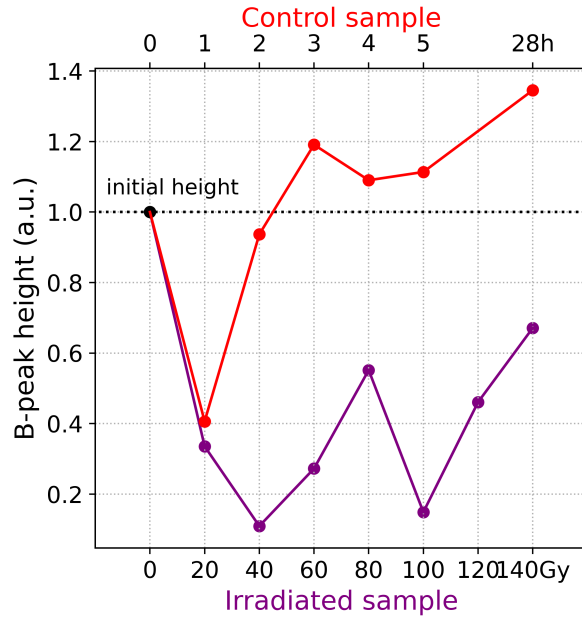


Figure 3.15: Height of the B-transition for the 711 with dose, in purple, and for 712 with time, in red.

the University of Bologna on the same type of  $\text{MAPbBr}_3$  single crystals suggest similar interpretation; it is known that PL in perovskites is mainly dominated by the excitonic radiative recombination, rather than by the free carrier recombination [6]. The PL peak of  $\text{MAPbBr}_3$  measured after the irradiation with X-ray photons shifts toward lower energies, suggesting that the excitons could be subjected to an increase of binding energy. As for the energy range, the high energy tail of the spectrum has been excluded, since it is affected by surface recombination; the spectrum below 2.2 eV has been instead extended to 2.1 eV, thanks to the absence of the B-transition.

The results are presented in figure 3.16.

The energy gap, the exciton binding energy and the linewidth have been extracted from the fit and reported in table 3.3. Compared with the values in table 3.1 of section 3.2.1,

Table 3.3: Parameters calculated from fitting of SPV data with Elliott's absorption formula

X-ray dose	$E_g$ (eV)	$E_b$ (meV)	$\Gamma$ (meV)
0 Gy	$2.326 \pm 0.003$	$52 \pm 2$	$40.7 \pm 0.7$
200 Gy	$2.301 \pm 0.002$	$72 \pm 2$	$29.4 \pm 0.8$

the 0Gy curve can be fitted with the exact same binding energy and energy gap, which

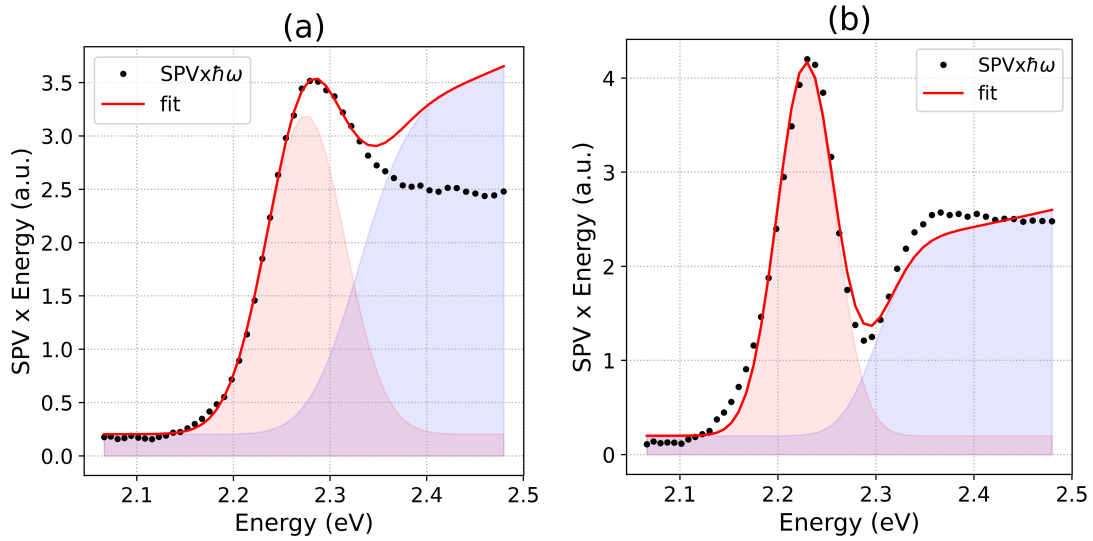


Figure 3.16: SPV data multiplied by the energy of the 613 irradiated sample; data and fit are represented by the black dots and the red solid line respectively, for the 0Gy curve (a), and for the 200Gy curve (b). The red and the blue area display the excitonic and the continuum contribution to the total absorption.

are equal to  $52 \pm 2$  meV and to  $2.326 \pm 0.003$  eV, respectively; the small difference in the linewidth can be attributed to the different energy range chosen for the fitting procedure.

The best fit for the 200Gy curve yields to a smaller energy gap, equal to  $2.301 \pm 0.002$  eV, and to a larger exciton binding energy, equal to  $72 \pm 2$  meV.

In order to graphically test the validity of the model and of the calculated parameters, the energy gap, the exciton binding energy and the linewidth have been slightly changed and compared in figures 3.17 with respect to the ones extracted by the fit.

According to the fit parameters reported in table 3.3, the exciton binding energy is subjected to an increase of about 20 meV, after deposition of 200Gy X-ray dose.

As described in section 1.3.3, the binding energy of an exciton can be described within the Wannier-Mott model and therefore depends on the reduced exciton mass  $\mu$  and on the dielectric function  $\epsilon_r$  of the material, through the relation 1.4, reported here again for clarity:

$$E_b = \frac{R_0\mu}{m_0\epsilon_r^2} \quad (3.2)$$

In perovskites there are multiple physical processes which can affect dielectric polarization; such processes involve the optical response  $\epsilon^{optical}$  in the high frequency part, and the ionic contribution  $\epsilon^{ionic}$  in the THz range, given by the response of the lattice vibrations and proportional to the polarity of the chemical bonds; furthermore, the orientation

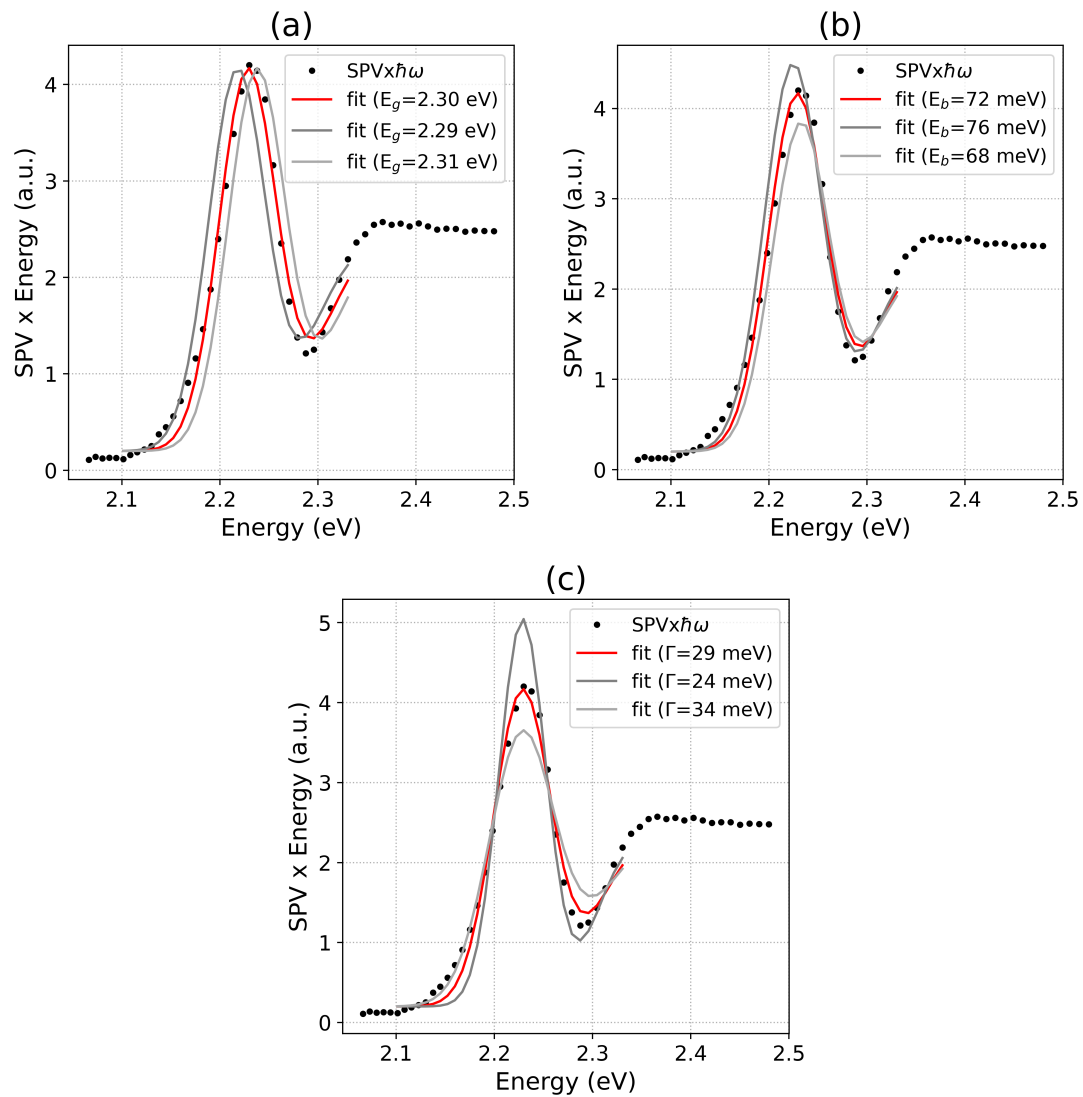


Figure 3.17: In black, the experimental data for 260Gy, in solid red, the fitted curve with calculated parameters, in solid gray, the simulated curves obtained by a small change of  $E_g$ ,  $E_b$  and  $\Gamma$  in (a), (b) and (c), respectively.

of the dipolar species  $\epsilon^{dipoles}$  in the GHz and MHz range, and the space charges  $\epsilon^{sc}$ , resulting from both ionic and electronic species in the low frequency range, contribute to the total dielectric function. Any modification in those contributions inside the crystal reflects in a change of the material polarizability.

For instance, the X-ray photons could have modified in some way the ionic cage, by changing the bond between the lead and the bromide. In literature there are some studies on the effects induced by X-ray radiation on perovskites: Wang [45] and Anaya et al. [46] observed the formation of metallic lead with X-ray photoelectron spectroscopy. The authors suggested that the formation of metallic lead after exposure to X-rays could be attributable to the reduction of the Pb<sup>2+</sup> in to Pb<sup>0</sup> and linked to the oxidation of Br<sup>-</sup> in to Br<sub>2</sub>, which can be easily desorbed from the surface. This reaction could have, for example, changed the dielectric function by introducing Br-vacancies, left by the desorption of the Br<sub>2</sub>, or by forming clusters of Pb<sup>0</sup>. The change in the lead-bromide ionic cage could have affected the dielectric response from the methylammonium cation; as suggested by Anusca et al. [64], MA-dipoles are able to orient themselves in the proximity of a lead vacancy or of a halogen vacancy. The ordering of the organic cation reduces the ability to screen the mobile charge and this results in a decreased dielectric function.

### 3.3.2 Photocurrent spectroscopy

All data reported in the following section have been acquired with the same setting parameters described in section 3.2.3. The photocurrent spectroscopy results for the 711 irradiated sample and for the 712 control sample are presented in figure 3.18 (a) and (b).

The nomenclature for the features characterizing the photocurrent spectra has been

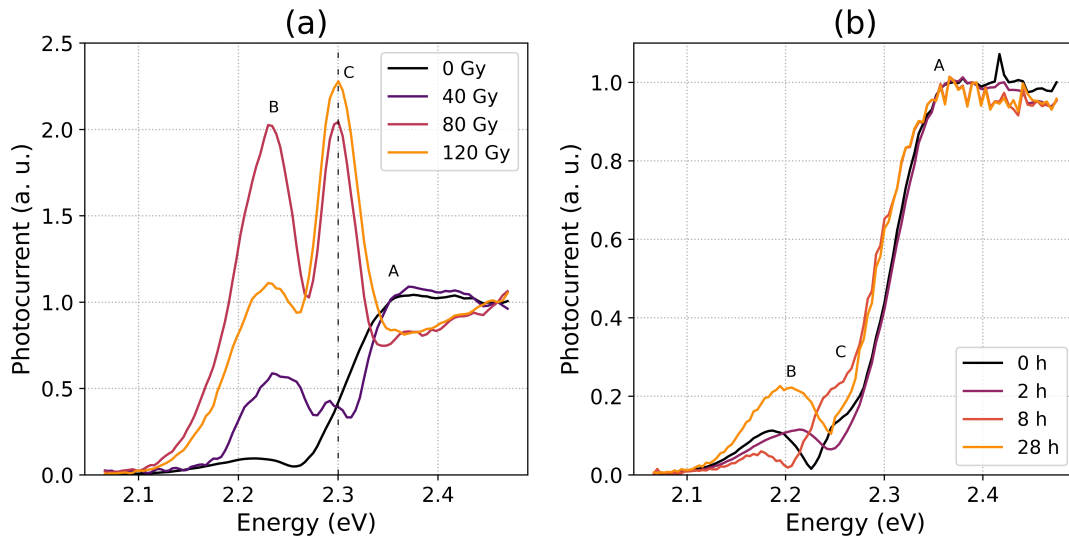


Figure 3.18: (a): PC spectra of the 711 irradiated sample after exposure to X-rays in 20Gy steps, at selected doses, namely the ones at 0, 40, 80 and 120Gy. (b): PC spectra of the control 712 sample at 0, 2, 4 and 28 hours.

chosen due to the similar trend of those features with respect to the SPV spectra, reported in figure 3.12.

The intensity of the B-transition oscillates randomly with the deposited dose. The C-transition appears at around 2.30 eV after the 40Gy dose has been deposited and increases with the deposited dose.

The 712 photocurrent spectra are characterized as well by the B-transition at lower energies, while the C-transition is only slightly visible.

The position in energy of the below band gap peak for the control sample 712 is not constant in time, ranging from 2.17 eV to 2.22 eV; this fact corroborates the hypothesis that the different position of the below band gap peak in photocurrent with respect the surface photovoltage could be affected by charge transport mechanisms such as the motion and accumulation of mobile ions, as suggested in section 3.2.3.

Figure 3.19 presents the recovery of the 711 irradiated sample after 16 and 45 hours from the 140Gy deposited dose. The recovery of the sample shows that the C-transition disappears with time, going back to the initial value; at the same time, the B-transition

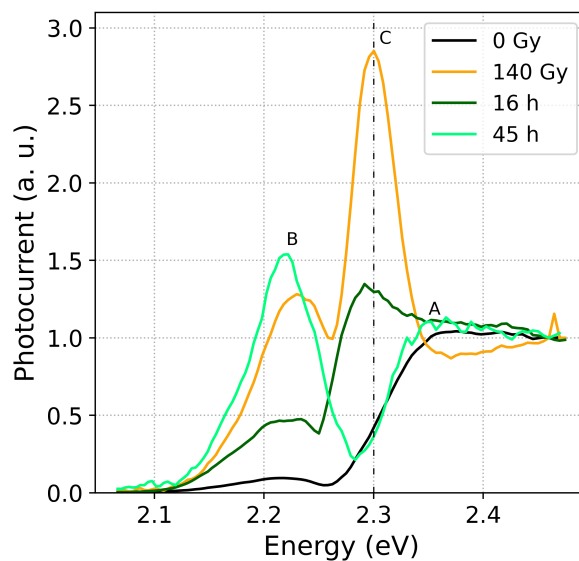


Figure 3.19: PC spectra of the 711 recovery after irradiation with 140 Gy x-ray dose. In black and yellow respectively, the spectra at 0 Gy and 140 Gy doses. In dark and light green the spectra after 16 and 45 h after the last deposited dose.

becomes more intense. Figure 3.20 displays the variation of the B-peak for the irradiated sample 711 and the control sample 712; the intensity of B behaves steadily with time while varying strongly with the deposition of X-rays.

### 3.3.3 Comparison between Surface photovoltage and Photocurrent measurements

The spectra of figure 3.21 compare the SPV signal, in blue, with the PC signal, in red, for 0 Gy, 40 Gy, 80 Gy and 120 Gy deposited doses, for the 711 sample.

The SPV and PC spectra display several differences; for all the doses, the position of peak B in the PC is shifted towards higher energies with respect to the SPV; as stated in section 3.2.4 and from comparison with the spectra of figure 3.18 (b), its different position could be related to the different transport mechanism involved in the photocurrent signal, and could be strongly affected by the accumulation of ions at the contacts.

The excitonic peak A\*, characteristic of the SPV spectra at 0 Gy, does not appear in the PC spectra at 0 Gy; as explained in section 3.2.4, this could be due to the ionic transport that reduces the mobility and the collection efficiency of charges.

The C-peak appears right after the deposition of a 40 Gy dose in the photocurrent spectra, while the new peak appears in SPV only at higher doses, here at 120 Gy, and located at lower energies. The difference in the energy position, in SPV around 2.23 eV, while

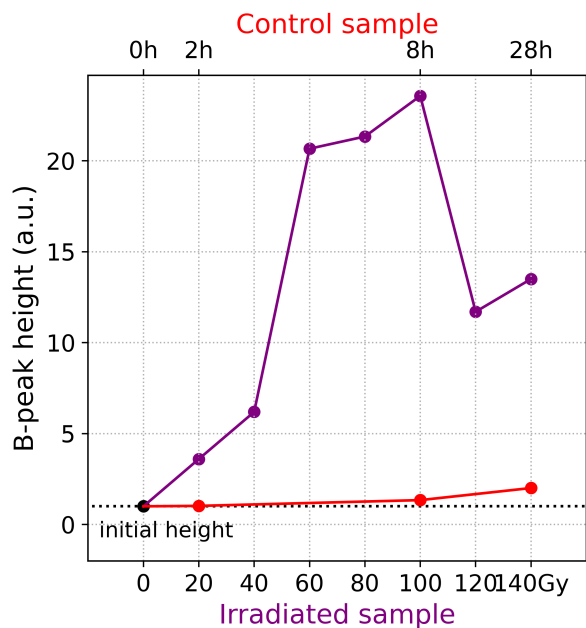


Figure 3.20: Variation of the B-peak height with increasing dose for the 711 irradiated sample in purple, and with time for 712 control sample, in red.

in PC around 2.30 eV, is consistent with the explanation of ionic transport affecting the position of the characteristic features.

Since in sample 613 (figure 3.13) the peak at position C is visible after the first deposition of 20Gy, it is reasonable to think that the height of that peak could be dependent on the sample growth. The presence of the below band gap peak B could have hindered the SPV signal coming from the the C transition, thus appearing much less resolved with respect to the same transition in sample 613.

Overall, despite all these differences between the photocurrent and the surface photovoltage signals, both spectra suggest that the exciton binding energy had increased after the deposition of the X-ray dose.

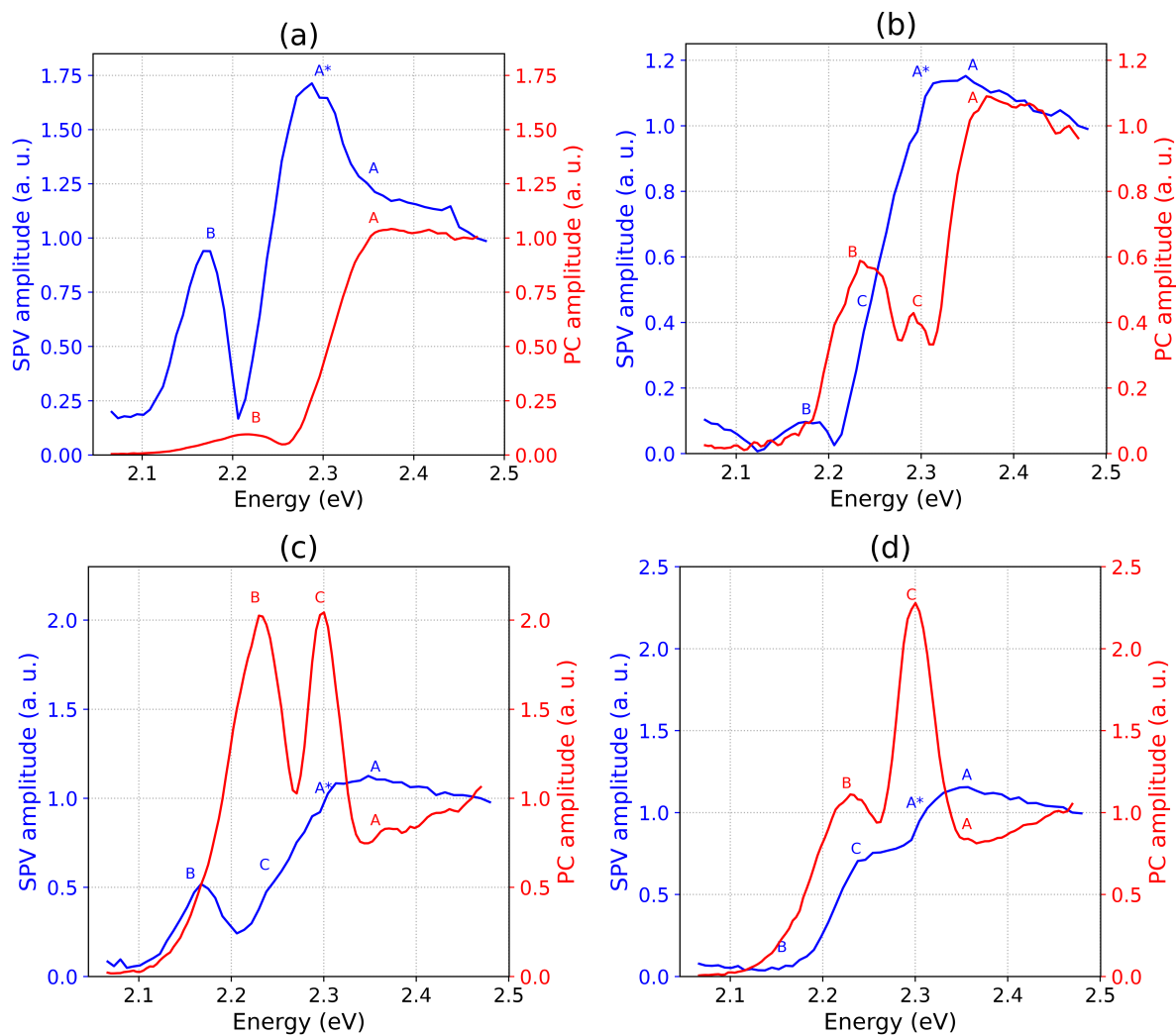


Figure 3.21: Comparison between the SPV spectra, in blue, and the PC spectra, in red, at 0Gy in (a), 40Gy in (b), 80Gy in (c) and 120Gy in (d) X-ray doses.

### 3.3.4 Discussion on the increase of exciton binding energy

Within the framework of the Wannier-Mott hydrogenic model, the exciton's binding energy depends on the dielectric function, which is mainly given by the ability of the lead-bromide cage and the methylammonium motion to screen the charge carriers interaction; this fact has been previously discussed and has been proposed to explain the observed changes in the exciton binding energy reported in section 3.3.1.

However, because of the large difference between the static dielectric constant  $\epsilon_s$  and the optical dielectric constant  $\epsilon_\infty$ , perovskites should be better described within the framework of polarons [65]; polarons in perovskites are believed to be responsible for the increase of carrier effective mass and the reduced mobility. Moreover, the polarization cloud around the electron and the hole modifies their attractive interaction, giving rise to non-hydrogenic exciton states.

As described in section 1.3.2, perovskites behave as polar materials, where electrons strongly interact with the longitudinal optical phonons, giving rise to a large Fröhlich coupling constant,  $\alpha$  [17].  $\alpha$  describes the strength of the electron-optical phonon and hole-optical phonon interaction:

$$\alpha_{e,h} = \sqrt{m_{e,h}e^4/2\hbar^2\epsilon_*^2E_{LO}} \quad (3.3)$$

where  $m_{e,h}$  is the bare effective carrier mass,  $1/\epsilon_* = 1/\epsilon_\infty - 1/\epsilon_0$  is the ionic screening of carriers and  $E_{LO}$  is the energy of the longitudinal optical phonons. In fact, perovskites in general are characterized by a large  $1/\epsilon_*$  and by a low LO phonon energy  $E_{LO}$ ; the effects of the ionic lattice is particularly relevant for bromide perovskite, where the ionicity of the Pb-Br bonds is higher with respect to the iodine perovskite and therefore polaronic effects are much more enhanced.

Excitons in polar materials should be better described by an hydrogen-atom model in a modified potential  $V(r)$  with respect to the classical Coulombic interaction; the relative energy levels have been calculated by Menéndez-Proupin et al. [66] for different choices of  $V(r)$ .  $V(r)$  has been found to significantly change the energy of the 1s transition with respect to the values calculated for a Coulombic potential.

Baranowki et al. [65] demonstrated how the properties of the exciton states change when the difference between  $\epsilon_s$  and  $\epsilon_\infty$  is significant (respectively  $\sim 20$  and  $\sim 5$ ) or small (respectively  $\sim 5$  and  $\sim 5$ ). The authors found that when  $\epsilon_s$  is very different from the optical dielectric constant, the exciton is bound more tightly, for each of the modified potentials  $V(r)$  considered.

Moreover, the soft lattice nature and strong electron-phonon coupling of perovskites

give rise to *self-trapped excitons* (STEs) [67]; STEs have been observed in halide crystals, condensed rare gases and organic molecular crystals. In these kind of materials, once the electrons and holes are photogenerated, they become self-trapped, by localizing themselves in a potential well introduced by a lattice distortion. The self-trapped state forms because it is more stable than the one in which the electron-hole pair would move, dragging the lattice distortion.

The presence of both free and localized excitons has been observed in perovskites [68, 69]. Mariano et al. [6] attributed two contributions to the photoluminescence spectrum of MAPbBr<sub>3</sub> thin film to two excitonic resonances: a free and a localized exciton; in particular, a localization of about 15 meV is observed between the localized and the free exciton.

An analogous mechanism could have occurred as a result of the X-ray deposition, that would explain the result of section 3.3.1. X-ray photons could have generated or increased lattice deformations; the consequent structural disorder appears as potential energy fluctuations, with maxima and minima, around which an electron and a hole can localize and form localized excitons; the reduced distance between the pair results in an increased binding energy. Thus, the increment of 20 meV of the exciton binding energy, reported in section 3.3.1, stems from the localization of the exciton around the crystal distortion.

The recover of the crystal after some hours from the last irradiation, observed from figures 3.14 and 3.19, suggests a dynamic behaviour of the crystal distortions, rather than fixed. So that when the lattice relaxes to the ground state after excitation, the crystal recovers the condition that it had prior the irradiation process.



# Conclusions

This thesis focused on the optoelectronic characterization of two perovskite-based materials. The first device is a MAPbI<sub>3</sub> thin film solar cell that has been characterized with the aim of improving its photovoltaic performances. The second perovskite-based material is a MAPbBr<sub>3</sub> single crystal, that has been characterized with surface photovoltage and photocurrent spectroscopy in order to test the effects of X-ray radiation on its optoelectronic properties.

The MAPbI<sub>3</sub> solar cells have been fabricated in a n-i-p planar structure and the main photovoltaic parameters have been extracted from the dark and from the illuminated I-V characteristic. The photovoltaic parameters reported for one of the MAPbI<sub>3</sub> solar cell, measured from the dark I-V curve, reveal that no significant current shunts or contact resistances affected the device. From the output curve of the illuminated cell, the power conversion efficiency of the forward and backward scan have been extracted. The large difference between the forward and backward I-V, with power conversion efficiency respectively equal to 7.7%, and 12.1%, shows that the solar cell is largely affected by hysteresis; the hysteresis is attributed to the motion and to the accumulation of slow ions. Because of hysteresis, the extracted values greatly depend on the scanning parameters and can lead to a misinterpretation of the results. Overall, the measured parameters are far below the state-of-the art which is now around 22% [70]; the lock-down in March 2020 due to the Covid-19 emergency, did not allow the follow-up of the planned activity, and the optimization and the radiation hardness tests of the prepared cells have not been carried out. To monitor the radiation hardness of the material, MAPbBr<sub>3</sub> single crystals have been chosen instead, for their interesting potential as X-ray detectors.

The MAPbBr<sub>3</sub> single crystals have been characterized via surface photovoltage (SPS) and photocurrent spectroscopy (PCS), with the aim to test their radiation hardness to X-ray photons; the main features (A, A\*, B and C) of the SPS and PCS spectra have been summed in the table 3.4, along with their typical energies, their behaviour with X-ray irradiation and their possible origin.

Table 3.4: Summary of the main features and their behaviour with X-ray deposition.

	<b>Typical energy</b>	<b>Behaviour with X-ray</b>	<b>Attributed to</b>
A	SPV: 2.35 eV PC: 2.35 eV	Constant.	Band-to-band absorption.
A*	SPV: 2.29 eV	Disappears after first 20Gy deposition.	Excitonic absorption ( $E_b = 52 \pm 2$ meV).
B	SPV: 2.17 eV PC: 2.17-2.21 eV	Varies randomly with deposition.	Defect state.
C	SPV: 2.23 eV PC: 2.30 eV	Increases with deposition, decreases with recovery.	Excitonic absorption ( $E_b = 72 \pm 2$ meV).

The main features of table 3.4 are discussed hereafter:

- The maximum of the band-to-band absorption A remains constant with the deposition of the X-ray photons.
- The below band-gap peak B, whose origin is still under investigation, has been attributed to a defect state, as suggested by the analysis of the amplitude and phase of SPS (figure 3.5). Its origin has been associated to an uncontrolled process, such as a stoichiometry unbalance between the MABr and the PbBr<sub>2</sub> precursors. Its sudden increase of intensity right after the contact deposition, illustrated in plot (b) of figure 3.4, has been attributed to the effect of high vacuum or to the diffusion of chromium atoms inside the perovskite layer, which increased the trap density related to the defect state. The decrease in the intensity of this feature, observed after 96h from the deposition, has been supposed to originate from a partial passivation induced by oxygen that is often quoted in literature [57, 58, 59]. A large and random variation has been registered after the deposition of the X-ray doses, which could have contributed to the disorder of the crystal, visible from figures 3.15 and 3.20.
- The strong SPV signal A\* near the band gap, prior to X-ray irradiation, has been assigned to the excitonic absorption; an exciton binding energy  $E_b$  equal to  $52 \pm 2$  meV for sample 613 has been calculated by fitting the experimental SPV spectra with the Elliott's absorption formula (figure 3.16 (a)). The extracted  $E_b$  for samples 711, 712, 613 are all comparable with the lower range of values found in literature for bromide perovskite single crystals [5]. After the deposition of the X-ray doses,

the exciton increased its binding energy, attested by the vanishing of feature A\* and by the appearing of the new feature C.

- The peak C that appears after irradiation has been assigned to an excitonic absorption with increased binding energy; the exciton binding energy has been calculated by fitting the SPV spectrum at 200Gy yielding a value of  $72 \pm 2$  meV in sample 613 (figure 3.16 (b)). The increase by 20 meV of the binding energy has been attributed to a localization of the electron-hole pair around lattice deformations introduced by the X-rays. The localization of excitons has been assigned to the polar nature of perovskites, whose relevance has been often underlined in literature [17, 66, 65]. A measurement of the dielectric function near the optical absorption energy right after the X-ray irradiation could be useful to test the validity of the hypothesis of X-rays affecting the polarizability of the material.

In conclusion, the surface photovoltage and the photocurrent spectroscopies have been successfully performed to test the effects of X-ray radiation on the MAPbBr<sub>3</sub> optoelectronic properties. In particular, the following three results should be highlighted:

- i. This is the first time, even if the presence of free and localized excitons has been previously reported in perovskites [6, 68, 69], that an increase of exciton binding energy has been observed following the irradiation with X-rays.
- ii. The recovery of the perovskite after some hours from the last dose at 140Gy has been observed from spectra 3.14 and 3.19, where the sample's absorption edge returns to its initial condition; this confirms the relatively high tolerance of the material to X-ray photons and thus the possibility to use it as active layer in commercially available X-ray detectors.
- iii. The surface photovoltage technique is able to correctly reproduce the absorption coefficient near the absorption edge of thick samples; the advantage of this technique applied to perovskite single crystals is that it allows to measure the full absorption spectrum without performing two distinct reflectance and transmittance spectra, and without having to thin the sample.



# Bibliography

- [1] <https://www.nrel.gov/pv/cell-efficiency.html>
- [2] Wei, H. et al. "Sensitive X-ray detectors made of methylammonium lead tribromide perovskite single crystals". *Nature Photonics* 10, 333-339 (2016).
- [3] Yakunin, S. et al. "Detection of X-ray photons by solution-processed lead halide perovskites". *Nature Photonics* 9, 444-449 (2015).
- [4] Marongiu, D. et al. "The role of excitons in 3D and 2D lead halide perovskites" *J. Mater. Chem. C* 7, 12006-12018 (2019).
- [5] Droseros, N. et al. "Photophysics of Methylammonium Lead Tribromide Perovskite: Free Carriers, Excitons, and Sub-Bandgap States". *Adv. Energy Mater.* 10, 1903258 (2020).
- [6] Mariano, F. et al. "The enhancement of excitonic emission crossing Saha equilibrium in trap passivated  $\text{CH}_3\text{NH}_3\text{PbBr}_3$  perovskite". *Commun Phys* 3, 41 (2020).
- [7] Goldschmidt, V. M. "Die Gesetze der Krystallochemie". *Naturwissenschaften* 14, 447-485 (1926).
- [8] Chen, Q. et al. "Under the spotlight: The organic-inorganic hybrid halide perovskite for optoelectronic applications". *Nano Today* 10, 355-396 (2015).
- [9] Wells, H. L. "Über die Cäsium - und Kalium- Bleihalogenoide". *Zeitschrift für anorganische Chemie* 3, 195-210 (1893).
- [10] Møller, C. K. "Crystal Structure and Photoconductivity of Cesium Plumbahalides". *Nature* 182, 1436 (1958).
- [11] Weber, D. " $\text{CH}_3\text{NH}_3\text{PbX}_3$ , ein Pb(II)-System mit kubischer Perowskitstruktur". *Zeitschrift für Naturforschung* 33b, 1443-1445 (1978).

- [12] Mitzi, D. B. "Synthesis, Structure, and Properties of Organic-Inorganic Perovskites and Related Materials". *Progress in Inorganic Chemistry*, ed. Karlin K. D. (1999).
- [13] Kojima, A. et al. "Organometal halide perovskites as visible-light sensitizers for photovoltaic cells". *Journal of the American Chemical Society* 131, 6050-6051 (2009).
- [14] Im, JH. et al. "6.5% efficient perovskite quantum-dot-sensitized solar cell". *Nanoscale* 3, 4088-4093 (2011).
- [15] Chung, I. et al. "All-solid-state dye-sensitized solar cells with high efficiency". *Nature* 485, 486-489 (2012).
- [16] Lee, M. M. et al. "Efficient Hybrid Solar Cells Based on Meso-Superstructured Organometal Halide Perovskites". *Science* 338, 643-647 (2012).
- [17] Herz, L. M. "Charge-Carrier Dynamics in Organic-Inorganic Metal Halide Perovskites". *Annu. Rev. Phys. Chem.* 67, 65-89 (2016).
- [18] Li, C. et al. "Formability of  $ABX_3$  (X=F, Cl, Br, I) halide perovskites". *Acta Crystallographica B* 68, 702-707 (2008).
- [19] Green, M. A. et al. "The emergence of perovskite solar cells". *Nature Photonics* 8, 506-514 (2014).
- [20] Toshniwal, A. et al. "Development of organic-inorganic tin halide perovskite: A review". *Solar energy* 149, 54-59 (2017).
- [21] Saliba, M. et al. "Cesium-containing triple cation perovskite solar cells: improved stability, reproducibility and high efficiency". *Energy Environ. Sci.* 9, 1989-1997 (2016).
- [22] Schmidt-Mende, L. et al. "Organic and Hybrid Solar Cells". *De Gruyter Graduate* (2016).
- [23] Chen, C. et al. "Elucidating the phase transitions and temperature-dependent photoluminescence of MAPbBr<sub>3</sub> single crystal". *J. Phys. D: Appl. Phys.* 51, 045105 (2018).
- [24] Frost, J. M. et al. "Atomistic Origins of High-Performance in Hybrid Halide Perovskite Solar Cells". *Nano Lett.* 14, 2584-2590 (2014).

- [25] Brivio, F. et al. "Structural and electronic properties of hybrid perovskites for high-efficiency thin-film photovoltaics from first-principles". *APL Mater.* 1, 042111 (2013).
- [26] Buin, A. et al. "Halide-Dependent Electronic Structure of Organolead Perovskite Materials". *Chem. Mater.* 27, 4405-4412 (2015).
- [27] Shi, T. et al. "Unipolar self-doping behavior in perovskite  $CH_3NH_3PbBr_3$ ". *Appl. Phys. Lett.* 106, 103902 (2015).
- [28] Motta, C. et al. "Revealing the role of organic cations in hybrid halide perovskite  $CH_3NH_3PbI_3$ ". *Nat. Comm.* 6, 7026 (2015).
- [29] Mosconi, E. et al. "Electronic and optical properties of  $MAPbX_3$  perovskites (X=I, Br, Cl): a unified DFT and GW theoretical analysis". *Phys. Chem. Chem. Phys.* 18, 27158-27164, (2016).
- [30] Park, C. H. et al. "First-principle study of the structural and the electronic properties of the lead-halide-based inorganic-organic perovskites  $(CH_3NH_3)PbX_3$  and  $CsPbX_3$  (X=Cl, Br, I)". *J. Korean Phys. Soc.* 44, 889-893 (2004).
- [31] Kulkarni, S. A. et al. "Band-gap tuning of lead halide perovskites using a sequential deposition process". *J. Mater. Chem. A* 2, 9221-9225 (2014).
- [32] Elliott, R. J. "Intensity of Optical Absorption by Excitons" *Physical Review* 108, 1384 (1957).
- [33] Saba, M. et al. "Correlated electron-hole plasma in organometal perovskites" *Nat. Commun.* 5, 5049 (2014).
- [34] Glaser, T. et al. "Infrared Spectroscopy Study of Vibrational Modes in Methylammonium Lead Halide Perovskites". *J. Phys. Chem. Lett.* 6, 2913-2918 (2015).
- [35] Song, Z. et al. "Pathways toward high performance perovskite solar cells: review of recent advances in organo-metal halide perovskites for photovoltaic applications". *J. Photon. Energy* 6, 022001 (2016).
- [36] Boyd, C. C. et al. "Understanding Degradation Mechanisms and Improving Stability of Perovskite Photovoltaics". *Chem. Rev.* 119, 3418-3451 (2019).
- [37] Zhao, Y. et al. "Recent Progress in High-efficiency Planar-structure Perovskite Solar Cells". *Energy Environ. Mater.* 2, 93-106 (2019).

- [38] Yang, S. et al. "Organohalide Lead Perovskites: More Stable than Glass under Gamma-Ray Radiation". *Adv. Mater.* 31, 1805547 (2019).
- [39] Lang, F. et al. "Radiation Hardness and Self-Healing of Perovskite Solar Cells" *Adv. Mater.* 28, 8726-8731 (2016).
- [40] Kim, J. et al. "The Role of Intrinsic Defects in Methylammonium Lead Iodide Perovskite". *J. Phys. Chem. Lett.* 5, 1312-1317 (2014).
- [41] Yin, W-J et al. "Unique Properties of Halide Perovskites as Possible Origins of the Superior Solar Cell Performance". *Adv. Mater.* 26, 4653-4658 (2014).
- [42] Noh, J. H. et al. "Chemical Management for Colorful, Efficient, and Stable Inorganic–Organic Hybrid Nanostructured Solar Cells". *Nano Lett.* 13, 1764-1769 (2013).
- [43] Kim, G. Y. et al. "Large tunable photoeffect on ion conduction in halide perovskites and implications for photodecomposition". *Nature Mater.* 17, 445-449 (2018).
- [44] Zhao, L. et al. "Redox Chemistry Dominates the Degradation and Decomposition of Metal Halide Perovskite Optoelectronic Devices". *ACS Energy Lett.* 1, 595-602 (2016).
- [45] Wang, C. et al. "Environmental Surface Stability of the MAPbBr<sub>3</sub> Single Crystal". *J. Phys. Chem. C* 122, 3513-3522 (2018).
- [46] Anaya, M. et al. "Origin of Light-Induced Photophysical Effects in Organic Metal Halide Perovskites in the Presence of Oxygen". *J. Phys. Chem. Lett.* 9, 3891-3896 (2018).
- [47] Cappel, U. B. et al. "Partially Reversible Photoinduced Chemical Changes in a Mixed-Ion Perovskite Material for Solar Cells". *ACS Appl. Mater. Interfaces* 9, 34970-34978 (2017).
- [48] Amari, A. et al. "Optimization of the Growth Conditions for High Quality CH<sub>3</sub>NH<sub>3</sub>PbBr<sub>3</sub> Hybrid Perovskite Single Crystals". *Cryst. Growth Des.* 20, 1665-1672 (2020.)
- [49] Donchev, V. "Surface photovoltage spectroscopy of semiconductor materials for optoelectronic applications". *Mater. Res. Express* 6, 103001 (2019).

- [50] Kronik, L. et al. "Surface photovoltage phenomena: theory, experiment, and applications". *Surface Science Reports* 37, 1-206 (1999).
- [51] Datta, S. et al. "Electroreflectance and surface photovoltage spectroscopies of semiconductor structures using an indium–tin–oxide-coated glass electrode in soft contact mode". *Review of Scientific Instruments* 72, 177 (2001).
- [52] Wenger, B. et al. "Consolidation of the optoelectronic properties of  $\text{CH}_3\text{NH}_3\text{PbBr}_3$  perovskite single crystals". *Nat. Commun.* 8, 590 (2017).
- [53] DeVore, H. B. "Spectral Distribution of Photoconductivity". *Phys. Rev.* 102, 86-91 (1956).
- [54] Cavalcoli, D. et al. "Surface photovoltage spectroscopy - method and applications". *Phys. Status Solidi (c)*, 7, 1293-1300 (2010).
- [55] Ambrosio, F. et al. "Charge localization and trapping at surface in lead-iodide perovskites: the role of polarons and defects". *J. Mater. Chem. A*, 8, 6882 (2020).
- [56] Deretzis, I. et al. "Atomistic origin of  $\text{CH}_3\text{NH}_3\text{PbI}_3$  degradation to  $\text{PbI}_2$  in vacuum". *Applied Physics Letters* 106, 131904 (2015).
- [57] Zhang, Z. et al "Natural passivation of the perovskite layer by oxygen in ambient air to improve the efficiency and stability of perovskite solar cells simultaneously". 88, 106007 (2021)
- [58] Motti, S. G. et al. "Photoinduced Emissive Trap States in Lead Halide Perovskite Semiconductors". *ACS Energy Lett.* 1, 726-730 (2016).
- [59] Zhou, Y. et al. "Mechanisms of Oxygen Passivation on Surface Defects in  $\text{MAPbI}_3$  Revealed by First-Principles Study". *J. Phys. Chem. C* 124, 3731-3737 (2020).
- [60] Levine, I. et al. "Deep Defect States in Wide-Band-Gap  $\text{ABX}_3$  Halide Perovskite". *ACS Energy Lett.* 4, 1150-1157 (2019).
- [61] Barnea-Nehoshtan, L. et al. "Surface Photovoltage Spectroscopy Study of Organo-Lead Perovskite Solar cells". *J. Phys. Chem. Lett* 5, 2408-2413 (2014).
- [62] Sutter-Fella, C. M. et al. "Band Tailing and Deep Defect States in  $\text{CH}_3\text{NH}_3\text{Pb}(\text{I}_{1-x}\text{Br}_x)_3$  Perovskites As Revealed by Sub-Bandgap Photocurrent". *ACS Energy Lett.* 2, 709-715 (2017).

- [63] Lafalce, E. et al. "Role of Intrinsic Ion accumulation in the Photocurrent and Photocapacitive Response of MAPbBr<sub>3</sub>". *ACS Appl. Mater. Interfaces* 8, 35447-35453 (2016).
- [64] Anusca, I. et al. "Dielectric Response: Answer to Many Questions in the Methylammonium Lead Halide Solar cell Absorbers". *Adv. Energy Mater.* 17, 1700600 (2017).
- [65] Baranowski, M. et al. "Excitons in Metal-Halide Perovskite". *Adv. Energy Mater.* 10, 1903659 (2020).
- [66] Menéndez-Proupin, E. et al. "Nonhydrogenic exciton spectrum in perovskite CH<sub>3</sub>NH<sub>3</sub>PbI<sub>3</sub>". *Phys. status solidi (RRL)* 9, 559-563 (2015).
- [67] Li, S. et al. "Self-Trapped Excitons in All-Inorganic Halide Perovskites: Fundamentals, Status, and Potential Applications". *J. Phys. Chem. Lett.* 10, 1999-2007 (2019).
- [68] He, H. et al. "Exciton localization in solution-processed organolead trihalide perovskites". *Nat. Commun.* 7, 10896 (2016).
- [69] Shi, J. et al. "Identification of high-temperature exciton states and their phase-dependent trapping behaviour in lead halide perovskites". *Energy Environ. Sci.* 11, 1460-1469 (2018).
- [70] Jiang, J. et al. "Improvement in solar cell efficiency based on the MAPbI<sub>3</sub> films extracted by a mixed anti-solvent". *Appl. Phys. Lett.*, 117, 203901 (2020).